Roles of interstitial carbon on transgranular fatigue crack resistance of ferritic steels

リ, ボチン

https://doi.org/10.15017/1866299

出版情報：Kyushu University, 2017, 博士（工学）, 課程博士
バージョン：
権利関係：

Roles of interstitial carbon on transgranular fatigue crack resistance of ferritic steels

A dissertation submitted to the faculty of engineering

Graduate school, Kyushu University, Japan

For the degree of doctor of philosophy

presented by

LI BOCHUAN

August 2017

Contents

Abstract

The fatigue problem gradually attracts increasing attention with the improvement of the scientific technologies and many researchers in the world attempts to enhance the fatigue properties of materials by using various kinds of methodologies, such as transformation-induced crack closure mechanism for transformation-induced plasticity (TRIP) steel, shot peening (SP) for material surface, grain size reduction, dynamic strain aging (DSA) phenomenon and etc. In terms of DSA, it is one of the most important conventional methods used for improving the fatigue strength, especially for the fatigue limit, through strengthening the material after plastic deformation.

Simply, the mechanism of DSA can be explained as the mutual effect between the moving dislocation and solute atoms. Actually, many controlling factors can have a notable influence on DSA phenomenon. To be exact, temperature dependence of DSA have already been investigated for various kinds of materials with DSA capacity in the past decades, while the solute atom concentration dependence of DSA, such as carbon and nitrogen atoms, is barely

examined. Hence, this thesis has mainly focused on the influence of solute carbon content on fatigue performance of ferritic steels with single ferrite phase.

To this end, fundamental researches were carried out to examine the characteristics of ferritic steels before, during and after the corresponding tests, for instance, Vickers hardness, fracture surface morphologies, fatigue crack propagation behaviors and etc. To measure the fracture surface morphologies, the scanning electron images and three-dimensional reconstruction software were used to the presented study and Replica technique with optical microscope was selected to catch the fatigue crack propagation path. Most crucially, the solid-solution treatment methodology was adopt to produce the ferritic steels with different controlled solute carbon contents.

This thesis outlines our findings in evaluating the solute carbon content dependence of fatigue limit with micro-notch and understanding the fatigue mechanism of crack growth behavior in different solute carbon concentrations, and the results show that as following briefly:

1) The threshold stress intensity factor range ΔK_{th} of Fe-0.017C alloy with the solute carbon concentration 0.017% reveals remarkably 40.5% higher than the predicted result of Murakami equation due to the stronger DSA effect in the grain interior.

2) The threshold stress intensity factor ranges ΔK_{th} of five ferritic steels with different solute carbon contents varying from 0% to 0.017% increased firstly

steeply due to DSA effect in the grain interior and then moderately as a result of uncontrolled carbon segregation to grain boundary (GBs), strengthening of solute poor zone at the vicinity of GBs.

3) Different controlling factors dominate the stronger fatigue strength of Fe-0.017C steel at different temperatures compared with interstitial- free (IF) steel. At room temperature (RT), Solid solution hardening and DSA hardening are the crucial factors, while three kinds of hardening mechanisms including under-aged precipitation hardening play a key role in ΔK_{th} at 333 K. Comparatively, the extent of asperity of fracture surface, leading RICC contribution to ΔK_{th}, and over-aged precipitation hardening result in stronger fatigue strength of Fe-0.017C steel than IF steel at 433 K.

The results of our studies indicate that solute carbon concentration is likely to play a notable role in the fatigue strength of notched or cracked specimen at least at temperature below 333K and it should be an effective dominant parameter to further improve the fatigue strength. Additionally, Suppression of the cementite precipitation, such as adding Si, can be hopeful to maintain the strong fatigue strength at elevated temperature. Overall, all the fundamental results in this thesis can enrich the knowledge to understand the DSA mechanism for fatigue strength and provide further research direction for material manufacture.

Keyword: dynamic strain aging; threshold stress intensity factor ranges; solute carbon concentration; elevated temperature; precipitation hardening;

List of tables

List of figures

Nomenclature

σ_{w0}	Fatigue limit of smooth specimen
σ_b	Tensile strength
ΔK_{th}	Threshold stress intensity factor range
$\sqrt{area}$	The square root of the area obtained by projecting the flaw onto a plane perpendicular to the loading axis direction
$\Delta K_{\mathrm{th\_pre}}$	The predicted fatigue threshold by using Murakami equation
I	The predicted error

CHAPTER 1. General introduction

1.1 Research background of this study

The steels, such as the Fe-C alloy, are the most popular materials used in the mechanical structure, such as in vehicle body described in Fig. 1.1 [1]. More specifically, many kinds of Fe-C alloys, such as multiphase steels, dual phase steels and high strength low alloy steels, are employed. In terms of these mechanical structures, although there are varieties of fracture factors which can lead to its final fracture, fatigue fracture significantly predominates [2]. In fact, due to the higher requirement for high reliability, convenience, environment-friendliness and low energy consuming in practical engineering, fatigue problems attract more and more attention. Therefore, many researchers proposed numerous mechanical methods and fatigue life models to evaluate the fatigue strength under different loading condition [3-5] or with different material defects [6-8]. However, even though these methods or models are precise enough, fatigue life scatter always exists due to a large amount of factors, such as the intrinsic defects size and inhomogeneous material properties in microscopic scales. Hence, another viewpoint from material science is employed to try to deal with fatigue problem and used to increase the fatigue performance, such as fatigue limit σ_{w0}, of materials and mechanical components [9]. More specifically, fatigue limit is one of the most important design parameters under which the fatigue life is infinite and one empirical equation is used to quantify the relationship between the tensile strength and fatigue limit directly [7]:

$$\sigma_{w0} = k\sigma_B \tag{1.1}$$

where σ_{w0} and σ_B are the fatigue limit and tensile strength in MPa. The empirical coefficient k value usually varies from 0.4 to 0.6 [7]. That is to say, there is a positive correlation between tensile strength and fatigue limit based on Eq. (1.1) and traditional methods in material science devoted to enhancing the tensile strength drastically so that the fatigue limit could be improved concomitantly [10-12]. However, in most cases, the tension properties of materials are usually satisfied with the design requirement, while only fatigue performance needs further improvement as Eq. (1.1) is not necessarily applicable to high strength steels or hard steels [7, 13]. Obviously, a large proportion of tension properties is not taken full advantage and manufacturing cost is increased by using the conventional methods.

The reason, leading to strong tensile strength with poor fatigue limit, is as a result of only attention to overall strength and ignorance of local strength in materials. More specifically, fatigue cracks always initiates and propagates along the locally weaker path or zone, especially under low stress level [7, 9, 12]. For example in one dual phase with ferrite/martensite phases as shown in Fig. 1.2, the fatigue crack usually initiates in the ferrite phase or in the interface between ferrite phase and martensite phase (hard phase). After crack initiation, fatigue crack prefers to grow in the ferrite phase rather than in hard phase as a result of retardation influence from hard phase [14]. Namely, local strength play a key role in fatigue performance of materials rather than overall strength. In fact, many researchers tries to enhance the local strength to improve the fatigue strength directly by using a large variety of material science techniques [15-22]. For instance, Koyama [15, 18] studied the influence of the location of cementite segregation in iron on fatigue crack propagation rate by using intergranular and transgranular cementite precipitation steels. It was clearly found that both the intergranular and transgranluar cementite acted as an obstacle against short fatigue crack growth. Therefore, a certain degree of cementite precipitation can be one of effective means to raise the fatigue crack resistance to some extent. Moreover, transformation-induced plasticity (TRIP) and twinning-induced plasticity (TWIP) are another two effective techniques to improve the crack closure level of fatigue crack [12, 17-19]. It was commonly believed that the material volume after phase transformation, e.g. transformation from austenite to martensite, would increase so that it would compress the wake of crack front and lead to crack closure in advance [19].

In addition, dynamic strain aging (DSA), described as the interaction between the dislocation and interstitial solute atoms, can be also used to strengthen the material locating the plastic zone in front of the crack tip [21, 23]. More specifically, solute atom can either segregate to grain boundary (GB) or diffuse to dislocation to form Cottrell atmosphere preventing further dislocation movement called as strain aging. In other words, once the dislocation emits from fatigue crack tip, it would be temporarily arrested by obstacles and pinned by solute atoms. Hence, it is necessary to investigate the influence of these factors (i.e. strain aging) from the viewpoint of metallurgical perspective so that the fatigue strength can be controlled and enhanced to some extent.

1.2 Review of dynamic strain aging

In terms of DSA, the aging phenomenon happens concurrently with straining. Therefore, it is reasonable to correlate it with effective strain rate. It is usually observed that DSA can even occurs at room temperature under slow strain rate meaning low dislocation velocity and improve the fatigue performance to some extent [24]. With normal interstitial solute level for iron and ferritic steel, the DSA always proceeds at certain temperature varying from 373-573K under normal strain rate, while it may extent down to room temperature with high interstitial solute content [25]. In some certain cases, DSA is still appeared at 673-943K, namely, the segregation of carbon or nitrogen is still strongly effective at elevated temperature [24]. Under certain strain rate, the temperature ranges making DSA characteristics occur is called as DSA regime. As a consequence of DSA, the growth of hardness, yield strength and tensile strength can be usually observed. Compared with room temperature, DSA happens more rapidly at relatively high temperature due to the increase of solute atom diffusivity, which can make the solute atoms segregate to dislocation and pin it as soon as possible. When the DSA occurs, several generally physical manifestation are summarized as: serrations in stress-strain curve; negative strain rate sensitivity; blue brightness; strain localization, etc.

1.2.1 General characteristic in tension test

In general, the features for stress-strain curve of steel with DSA influence at different working temperatures are revealed in Fig. 1.3 [21]. At room temperature, smooth stress-strain curve is obtained, while serration or jerky flow, named as Portevin-Le Chatelier (PLC) effect, often occurs at elevated temperature as shown in Fig. 1.3 When the temperature is beyond the "DSA regime", the jerky flow disappears. Moreover, the strain hardening exponent is a little larger in DSA regime than that out of DSA regime due to strain-aging hardening and elongation to fracture drops in this regime which is consistent with results of many other steels [24].

1.2.2 Chemical composition effects

It is generally thought that the carbon and nitrogen are two primary elements controlling the DSA phenomenon although many other elements, such as oxygen and hydrogen [26, 27], can also be responsible for it. The strain aging hardening peak is eliminated when the nitrogen is removed from manganese steel although carbon still exists in steel as cementite. Probably, the small influence of carbon in these steels is because of low interstitial carbon concentration compared with nitrogen. However, although the solubility of carbon in steel is low, considerable DSA effects as a result of carbon do happen in some steels in tension test. In fatigue test, both nitrogen and carbon are demonstrated to improve the fatigue strength at elevated temperature around 450K, while the fatigue strength with only nitrogen influence seems to be much higher than that with both carbon and nitrogen. This phenomenon may be due to interaction between these two elements [24, 28].

1.2.3 Strain rate influence

A large number of studies about the effects of strain rate on DSA process quantitatively verifies that the change of strain rate alters the DSA regime in temperature scale. In microstructural scale, effective strain rate corresponds to the velocity of dislocation motion. If the temperature is too low or strain rate is too fast, the diffusivity of solute atoms such as solute carbon and nitrogen is too slow to catch the moving dislocation, while the dragging force from the Cottrell atmosphere disappears if the temperature is too high or the strain rate is too slow. Only when both the temperature and strain rate are moderate, the DSA process can occurs prominently [28]. Serrations in stress-strain curve is one of the most important characteristics in DSA process and the occurrence of serrations coheres with the situation when almost all effective moving dislocations are pinned by solute atoms during straining. Then, once further dislocation multiplication occurs, the stress for deformation will suddenly drop to some extent as new freshly dislocation can move free without the constraint of the Cottrell atmosphere. After pining the new freshly dislocation again, the required stress for further deformation increases again and serration reveals significantly. The vanish of serrations can happen at elevated temperature probably due to that solute atoms can move with the moving dislocation without large dragging force.

1.2.4 Fatigue characteristic

One of the probable reasons as for why fatigue limit, under which the fatigue life is infinite, exists at room temperature is due to dislocation locking by interstitial atoms in iron and ferritic steels [29] and it is concluded that DSA do contribute to fatigue performance by constricting the spread of fatigue damage. As discussed above, the best evidence for the DSA enhancing fatigue strength is the characteristic of positive temperature dependence [28] which is similar with that in tension test. Generally, a peak value in fatigue strength or fatigue limit can be obtained for iron and ferritic steel at temperature around 473-673K. With the increasing of strain rate or working frequency, the peak temperature will become higher. Although many studies about the DSA influence on fatigue strength or fatigue life have been investigated by changing the temperature, almost all the fatigue tests are carried out by using smooth specimen, namely, the DSA effects on fatigue crack initiation resistance and fatigue crack propagation resistance cannot be quantified separately.

1.3 The aim of this thesis

Generally, there are at least four controlling factors which affect the DSA influence during fatigue loading: solute atom diffusivity, solute atom concentration, waiting time for aging and the dislocation velocity [30]. Obviously, temperature paid much more attention is one of the most important parameters which can affect the strain aging, as it can increase diffusivity of solute atoms [30]. Comparatively, the influence of another important parameter on fatigue strength, the solute atom concentration, is only considered by a few references [31-33]. Specifically, three kinds of low carbon steels were used in the previous study [32], the first one only had solute nitrogen, the second one had both solute carbon and nitrogen and the last was neither. In the first and second materials, peak temperature existed where the fatigue life became largest, which manifested the dynamic strain aging (DSA) effect. Although the second one had the highest solute content in the three steels, its peak temperature however was higher than the first one due to the interaction between carbon and nitrogen. In addition, only two materials, with and without solute atoms, were used to make comparison to demonstrate the existence of strain aging [31, 33]. Distinctly, the quantitative evaluation about the effect of single interstitial solute element concentration on fatigue strength is absence. Furthermore, in practical engineering, specimen usually contains a large amount of scratches and inclusions corresponding to small crack problem and threshold stress intensity factor range for propagation of small crack ΔK_{th} appears to be more sensitive to micro-structural characteristics and material properties in front of crack tip [9, 34]. Accordingly, based on above consideration, DSA may have an outstanding effect on small crack threshold due to changing the material properties dynamically in front of crack tip. Therefore, this thesis mainly quantifies and concentrates on the correlation between the interstitial solute concentration and DSA effects on fatigue crack propagation resistance under different conditions by using iron steels with single ferrite phase.

1.4 Outline of this research

The thesis consists of six chapters. All chapters are arranged in order to achieve the main theme and objectives of the research work. The thesis is organized as follows:

Chapter 1 describes a general introduction of the research work. The motivation of this research is based on the current issues in material science to investigate how to improve the fatigue performance by using DSA effect during cyclic loading. Based on the further requirement for low energy consuming, safety, environment-friendliness, the fatigue performance of materials should be enhanced directly rather than improving the tensile properties of materials to increase the fatigue strength indirectly. As DSA characteristic can be utilized as one of effective means to make an improvement for the fatigue strength, it attracts much attention. However, almost all attention is paid to temperature dependence of DSA, while few studies about the influence of solute atom concentration are investigated. Therefore, this thesis mainly focuses on the iron steels with different interstitial solute carbon contents and investigates their fatigue crack propagation resistance, namely, the threshold stress intensity factor ranges of small crack under different conditions.

Chapter 2 firstly reveals the model steel preparation for five ferritic steel with different interstitial carbon contents varying from 0% to 0.017% and introduces the corresponding heat treatment for five steels in detail. Then, the tension tests under different strain rates from 2.5×10^{-5} s^{-1} to 1.0×10^{-2} s^{-1} for five ferritic steels are conducted. Besides the normal tension test, the Vickers hardness for static strain aging specimens after pre-strain 4% and 8%, respectively, is measured in different aging time. Finally, the dynamic strain aging is verified for four ferritic steels whose interstitial carbon content is larger than 0% at room temperature.

Chapter 3 reported the comparison of threshold stress intensity factor ranges of small notch by using Murakami's equation [7] between interstitial-free steel and Fe-C binary steel with interstitial carbon content 0.017%. Fatigue tests were carried out by using rotating bending fatigue machine with stress ratio R=-1 and frequency 50Hz. In the center of specimen, three kinds of micro-notches were introduced by using the FIB technique and drilling hole machine. The $\triangle K_{th}$ of both two materials were determined with notch size $\sqrt{area}$ 337μm and the prediction error of Fe-0.017C was around 40% higher than that of predicted results by using Murakami's equation, while the prediction error of IF steel was only around -9%. The outstanding transgranular fatigue crack propagation resistance probably was due to the influence of DSA contribution.

Chapter 4 illustrated the correlation between the $\triangle K_{th}$ and interstitial carbon content varying from 0% to 0.017% for five iron steels with single ferrite phase. The $\triangle K_{th}$ value, at first, increases significantly when carbon content was from 0% to 0.0021% and then moderately. With the increase of interstitial carbon concentration, the DSA influence to strengthen the material properties in front of crack tip gradually became saturation. In addition, when the solute carbon content was relatively low, intergranular fracture feature dominated the fatigue crack behavior, while transgranlur crack propagation behavior became popular step by step when carbon content was increased. This phenomenon was due to the carbon segregation to grain boundary. Lastly, as carbon segregated to grain boundary, the called solute poor zone in the vicinity of grain boundary was the weakest zone where micro-crack always initiated. As the carbon content grew, both the DSA influence and strength in solute poor zone were improved to some extent.

Chapter 5 compared both the tension and fatigue results at three temperatures between Fe-0.017C and IF steels. Furthermore, the mechanical properties of Fe-0.017C steel after corresponding heat treatments were also examined. The controlling factors that dominate the higher $\triangle K_{th}$ value in Fe-0.017C steel compared with IF steel were analyzed. Solid solution hardening and DSA hardening, resulting in PICC contribution to ΔK_{th}, is the crucial factor at RT, while three kinds of hardening mechanisms including under-aged precipitation hardening play a key role in ΔK_{th} at 333 K. Comparatively, the extent of asperity of fracture surface, leading RICC contribution to ΔK_{th}, and over-aged precipitation hardening result in stronger fatigue strength of Fe-0.017C steel than IF steel at 433 K. The main reason for the $\triangle K_{th}$ reduction is because of a large amount of cementite precipitation and DSA hardening disappearance, which results in the decrease of PICC influence.

Chapter 6 summarized the results obtained by the present studies, and all findings were described in the general conclusions.

1.5 List of appended paper during Ph.D period: include publication

[1] B. Li, M. Koyama, E. Sakurada, N. Yoshimura, K. Ushioda, H. Noguchi, Underlying interstitial carbon concentration dependence of transgranular fatigue crack resistance in Fe-C ferritic steels: The kinetic effect viewpoint, International Journal of Fatigue, 98 (2017) 101-110.

[2] B. Li, M. Koyama, E. Sakurada, N. Yoshimura, K. Ushioda, H. Noguchi, Potential Resistance to Transgranular Fatigue Crack Growth of Fe-C alloy with a Supersaturated Carbon Clarified through FIB Micro-notching Technique, International Journal of Fatigue, (2016).

[3] B. Li, M. Koyama, E. Sakurada, N. Yoshimura, K. Ushioda, H. Noguchi, Competitive effect of dynamic strain aging and precipitation on ΔKth characteristic of a carbon steel containing supersaturated solute carbon. Philosophical Magazine Letters. (Under review)

[4] B. Li, M. Koyama, E. Sakurada, N. Yoshimura, K. Ushioda, H. Noguchi, Temperature dependence of transgranular fatigue crack resistance in an interstitial free steel and Fe-C alloy with a supersaturated carbon: effects of dynamic strain aging and dynamic precipitation. International Journal of Fatigue

[5] B. Li, M. Koyama, H. Noguchi. Threshold stress intensity factor range of a mechanically-long and microstructually-short crack perpendicular to an interface with plastic mismatch. Engineering Fracture Mechanics. (Under review)

1.6 Reference

[1] W. J.Parsons, Light weighting of 2013 Cadillac ATS body structure, great designs in steel seminar, Livonia., (2012).
[2] N.E. Frost, K.J. Marsh, L.P. Pook, Metal fatigue, Courier Corporation, 1974.
[3] B. Li, C. Jiang, X. Han, Y. Li, A new approach of fatigue life prediction for metallic materials under multiaxial loading, International journal of fatigue, 78 (2015) 1-10.
[4] J. Mei, P. Dong, A new path-dependent fatigue damage model for non-proportional multi-axial loading, International Journal of Fatigue, 90 (2016) 210-221.
[5] Y. Wang, L. Susmel, The Modified Manson–Coffin Curve Method to estimate fatigue lifetime under complex constant and variable amplitude multiaxial fatigue loading, International Journal of Fatigue, 83 (2016) 135-149.
[6] S. Hamada, T. Kinoshita, K. Morishige, K. Hayashi, T. Ishina, H. Noguchi, Engineering definitions of small crack and long crack at fatigue limit under tensile mean stress and a prediction method for determining the fatigue limit of a cracked Mg alloy, International Journal of Fatigue, 56 (2013) 86-94.
[7] Y. Murakami, Metal fatigue: effects of small defects and nonmetallic inclusions: effects of small defects and nonmetallic inclusions, Elsevier, 2002.
[8] D. Sasaki, M. Koyama, H. Noguchi, Factors affecting hydrogen-assisted cracking in a commercial tempered martensitic steel: Mn segregation, MnS, and the stress state around abnormal cracks, Materials Science and Engineering: A, 640 (2015) 72-81.
[9] S. Suresh, Fatigue of materials, Cambridge university press, 1998.
[10] A. Di Schino, J. Kenny, Grain size dependence of the fatigue behaviour of a ultrafine-grained AISI 304 stainless steel, Materials Letters, 57 (2003) 3182-3185.
[11] H.-K. Kim, M.-I. Choi, C.-S. Chung, D.H. Shin, Fatigue properties of ultrafine grained low carbon steel produced by equal channel angular pressing, Materials Science and Engineering: A, 340 (2003) 243-250.
[12] S. Zaefferer, J. Ohlert, W. Bleck, A study of microstructure, transformation mechanisms and correlation between microstructure and mechanical properties of a low alloyed TRIP steel, Acta Materialia, 52 (2004) 2765-2778.
[13] M. Garwood, Interpretation of tests and correlation with service, American Society for Metals, 1951.
[14] K. Nakajima, T. Urabe, Y. Hosoya, S. Kamiishi, T. Miyata, N. Takeda, Influence of microstructural morphology and prestraining on short fatigue crack propagation in dual-phase steels, ISIJ international, 41 (2001) 298-305.
[15] M. Koyama, Y. Yu, J.-X. Zhou, N. Yoshimura, E. Sakurada, K. Ushioda, H. Noguchi, Elucidation of the effects of cementite morphology on damage formation during monotonic and cyclic tension in binary low carbon steels using in situ characterization, Materials Science and Engineering: A, 667 (2016) 358-367.
[16] Z.-J. Xi, M. Koyama, Y. Yoshida, N. Yoshimura, K. Ushioda, H. Noguchi, Effects of cementite morphology on short-fatigue-crack propagation in binary Fe–C steel, Philosophical Magazine Letters, 95 (2015) 384-391.
[17] C. Haase, O. Kremer, W. Hu, T. Ingendahl, R. Lapovok, D.A. Molodov, Equal-channel angular pressing and annealing of a twinning-induced plasticity steel:

Microstructure, texture, and mechanical properties, Acta Materialia, 107 (2016) 239-253.

[18] M. Koyama, Z. Zhang, M. Wang, D. Ponge, D. Raabe, K. Tsuzaki, H. Noguchi, C.C. Tasan, Bone-like crack resistance in hierarchical metastable nanolaminate steels, Science, 355 (2017) 1055-1057.

[19] Z. Zhang, M. Koyama, M. Wang, K. Tsuzaki, C. Tasan, H. Noguchi, Effects of lamella size and connectivity on fatigue crack resistance of TRIP-maraging steel, International Journal of Fatigue, (2017).

[20] J.-C. Kim, S.-K. Cheong, H. Noguchi, Residual stress relaxation and low-and high-cycle fatigue behavior of shot-peened medium-carbon steel, International Journal of Fatigue, 56 (2013) 114-122.

[21] S.-G. Hong, S.-B. Lee, The tensile and low-cycle fatigue behavior of cold worked 316L stainless steel: influence of dynamic strain aging, International Journal of Fatigue, 26 (2004) 899-910.

[22] S. Zabeen, M. Preuss, P. Withers, Evolution of a laser shock peened residual stress field locally with foreign object damage and subsequent fatigue crack growth, Acta materialia, 83 (2015) 216-226.

[23] V. Srinivasan, R. Sandhya, M. Valsan, K.B.S. Rao, S. Mannan, D. Sastry, The influence of dynamic strain ageing on stress response and strain-life relationship in low cycle fatigue of 316L (N) stainless steel, Scripta materialia, 37 (1997) 1593-1598.

[24] J. Baird, The effects of strain-ageing due to interstitial solutes on the mechanical properties of metals, Metallurgical Reviews, 16 (1971) 1-18.

[25] B. Brindley, J. Barnby, Dynamic strain ageing in mild steel, Acta Metallurgica, 14 (1966) 1765-1780.

[26] W.A. Curtin, D.L. Olmsted, L.G. Hector, A predictive mechanism for dynamic strain ageing in aluminium–magnesium alloys, Nature materials, 5 (2006) 875-880.

[27] S.I. Hong, Influence of dynamic strain aging on the apparent activation volume for deformation, Materials Science and Engineering, 76 (1985) 77-81.

[28] G. Sinclair, An investigation of the coaxing effect in fatigue of metals, in, DTIC Document, 1952.

[29] K. Mariappan, V. Shankar, R. Sandhya, G.P. Reddy, M. Mathew, Dynamic strain aging behavior of modified 9Cr–1Mo and reduced activation ferritic martensitic steels under low cycle fatigue, Journal of Nuclear Materials, 435 (2013) 207-213.

[30] G. Oates, D. Wilson, The effects of dislocation locking and strain ageing on the fatigue limit of low-carbon steel, Acta Metallurgica, 12 (1964) 21-33.

[31] A. Ferro, G. Montalenti, Fatigue of pure iron and of iron containing a small quantity of carbon after strain ageing, Philosophical Magazine, 8 (1963) 105-119.

[32] G.S. JC Levy, An investigation of strain aging in fatigue, in, DTIC Document, 1954.

[33] C. Sommer, H. Mughrabi, D. Lochner, Influence of temperature and carbon content on the cyclic deformation and fatigue behaviour of α-iron. Part I. Cyclic deformation and stress–behaviour, Acta materialia, 46 (1998) 1527-1536.

[34] M. Koyama, Z.-J. Xi, Y. Yoshida, N. Yoshimura, K. Ushioda, H. Noguchi, Intergranular Fatigue Crack Initiation and Its Associated Small Fatigue Crack

Propagation in Water-quenched Fe–C Fully Ferritic Steel, ISIJ International, 55 (2015) 2463-2468.

1.7 Figures and tables

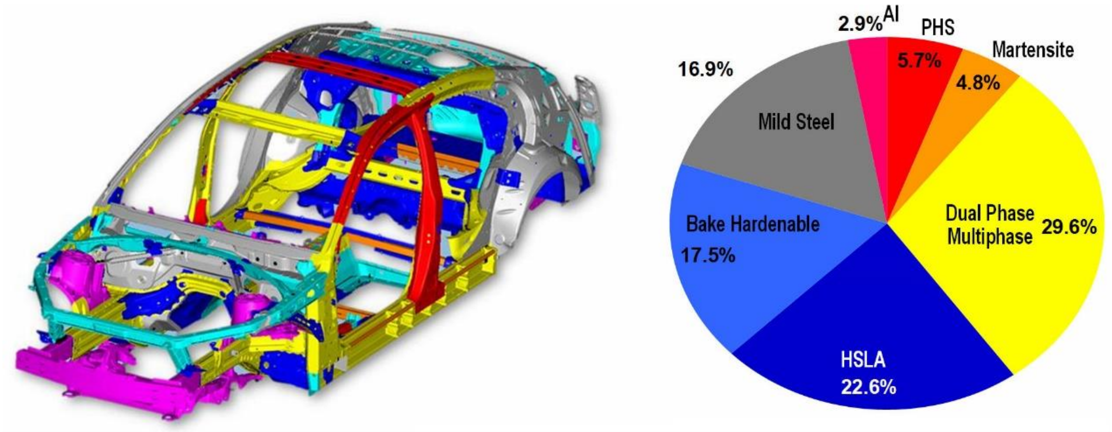

Fig. 1.1 The example for usage of Fe-C alloy in vehicle body [1]

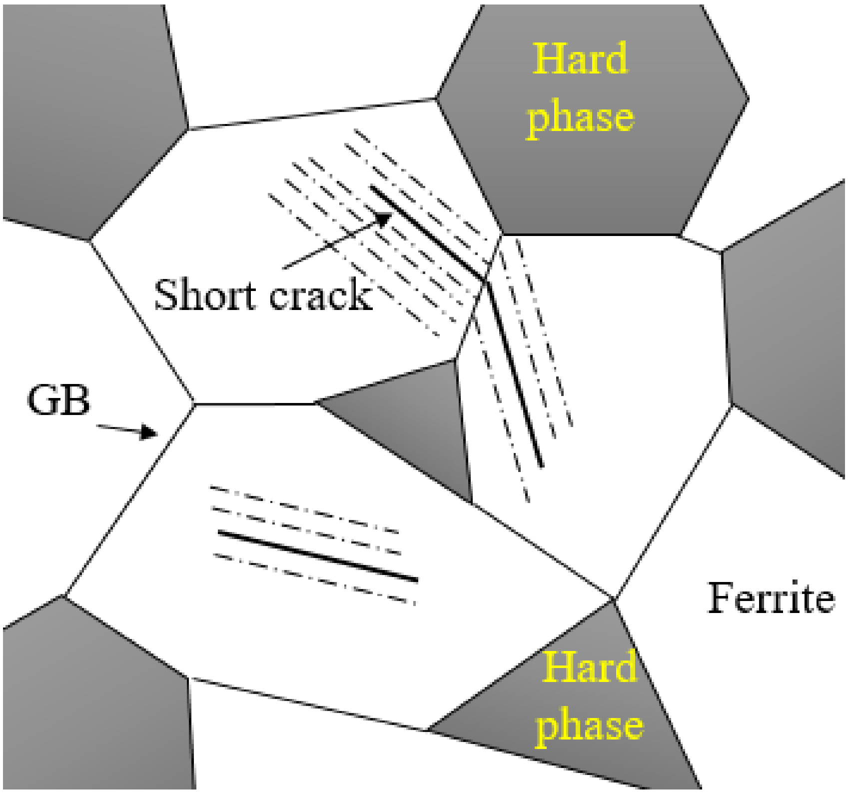

Fig. 1.2 The schematic of fatigue crack in ferrite/martensite dual phase

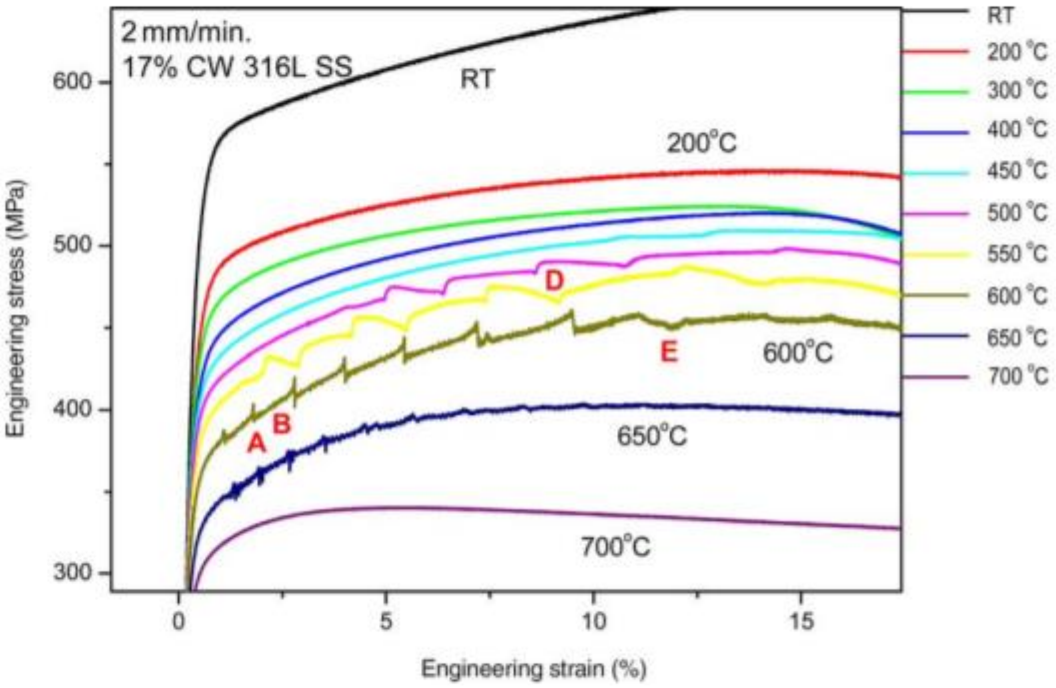

Fig. 1.3 The example for stress-curves of steels with DSA effect at different temperatures [21]

CHAPTER 2. Model steels selection and dynamic strain aging hardening verification at room temperature

2.1 Introduction

Solute atom content is one of the most important factor to affect the DSA hardening [1, 2] and the aim of this thesis is to investigate the interstitial carbon concentration dependence on transgranular fatigue crack resistance. Therefore, the corresponding materials used should be prepared specially so that the microstructure in all selected materials can be same except for the interstitial carbon content. Additionally, in order to eliminate the influence of complex microstructure on transgranular fatigue crack resistance, the microstructure of the materials should be as simple as possible. Lastly, before the fatigue test in this thesis, the corresponding tension tests should be carried out in advance so that the relative tension properties for presented materials, such as yield strength, ultimate strength (UTS) and elongation, could be investigated, which is better for understanding the fatigue performance in the following fatigue tests.

As discussed in Chapter 1 above, solute diffusivity, which are directly related to strain rate, plays notable role in DSA phenomenon [2-4]. Hence, the normal tension test in this chapter is carried out under different strain rates.

2.2 Model steels preparation

The materials totally used in this thesis are five iron steels with single ferrite phase as ferrite phase is one of the simplest microstructures. These five ferritic steels owns different interstitial carbon contents varying from minimum 0% to maximum 0.017% due to special heat treatments. The corresponding chemical compositions are illustrated clearly in Table 2.1. More specifically, although there is actually carbon content around 0.0019% in interstitial-free (IF) steel, all the interstitial carbon contents are exhausted as additional Ti is added into the steels to completely fix *C* and *N* to avoid interstitial solute atoms. Consequently, it is reasonable to deduce that there is no interstitial carbon in IF steel. Besides IF steel, all other four ferritic steels are prepared by the solid solution treatment. To be exact, as described in Fig. 2.1, the materials are heated to 973 *K* for 1h so that the microstructure is transformed to ferrite phase and then water-quench treatment is employed to room temperature so that the single ferrite phase can be saved at room temperature and suppress the formation of carbide or carbon clusters. Subsequently, all water-quenched materials were stored in a fridge at 186 K, except for the specimen preparation time and the fatigue test, to prevent precipitation and carbon segregation as much as possible. In addition, the optical images for these five ferritic steels after polishment and etching by 3% nitric acid alcohol solution are shown in Fig. 2.2, which reveals that the grain sizes of five steels are approximated which varies from 50 μm to 65 μm.

2.3 Tension test procedure

At first, tension tests for the five materials were conducted at different strain rates changing from 2.5×10^{-5} s^{-1} to 1.0×10^{-2} s^{-1} in air at room temperature (RT) to consider the dependence of strain rate on tension properties. Next, static strain aging capacity measurements of the five materials were accomplished by first pre-straining (4% and 8%), then unloading the tension and finally measuring the Vickers hardness with a 0.3 kg load during a period of around 2 days, which was close to the maximum fatigue time at RT. The geometries of all tension test specimen are same as revealed in Fig. 2.3.

2.4 Results and verification

2.4.1 Strain aging for tension tests at room temperature

The Stress-strain (S-S) curves of five steels under different strain rates at RT are displayed in Fig. 2.4. As the strain rate in IF steel increases, the induced stress for the same strain value increases, since the dislocation motion is controlled by thermal activation. Specifically, the higher strain rates would decrease the time for thermal activation, hence, more flow stress is required. A similar trend can also be seen for Fe-0.0021C steel. However, the opposite phenomenon occurs when the carbon concentration is higher than 0.0021% at lower strain rates. More specifically, at the same strain value, the flow stress is much larger for steels with carbon concentrations higher that Fe-0.0021C under the lowest strain rate than that under other strain rates. Additionally, the appearance of serrations can be observed in the Fe-0.0063C steel at the lowest strain rate, and in the Fe-0.0112C and Fe-0.017C steels at the two lowest strain rates, while no serration occurs for IF steel and Fe-0.0021C steel under any condition. The serration, which is one of the most obvious manifestation of DSA in the S-S curves, can be regarded as the repeated process of locking and unlocking mobile dislocations [5-8]. The relevant 0.2% proof stress and ultimate tensile strengths under different conditions are summarized in Fig. 2.5. Evidently, the 0.2% proof stress of all steels increases with the strain rate, which completely contradicts the tendency observed in high carbon content steels (Fe-0.0112C and Fe-0.017C) in terms of ultimate tensile strength, owing to higher DSA capacity in these two materials. For Fe-0.0063C steel, the ultimate tensile strength first reduces at a strain rate varying from $2.5\times10^{-5}s^{-1}$ to $1.0\times10^{-4}\ s^{-1}$, and then rises again with the strain rate, which clearly verifies the relationship between the strain rate dependence on the flow stress and the associated effect of DSA. Although Fe-0.0021C steel shows a similar trend as IF steel, the tensile strength change is negligible in the interval of strain rate from $1.0\times10^{-4}\ s^{-1}$ to $1.0\times10^{-3}\ s^{-1}$. Based on these experimental results, low carbon steel with higher carbon concentration from 0.0021% to 0.017% shows a negative strain rate sensitivity. Therefore, it demonstrates that DSA can occur at RT, at least for steels with carbon content higher than 0.0021% under a given strain rate.

2.4.2 Static strain aging of the five steel types at room temperature

Fig. 2.6 shows the variation of Vickers hardness with aging time for the five steels studied with pre-strains of 4% and 8%. Since IF steel does not have any solute carbon, its Vickers hardness does not change with aging time. On the other hand, the other four steels display a dependence of Vickers hardness on aging time. It can be seen from Fig. 2.6 that the Vickers hardness increases rapidly at the initial stage of aging for all solute carbon steels, and then the increasing rate gradually reduces under both pre-straining conditions, which has also been observed in other low carbon steels [9]. Although the Vickers hardness of all solute carbon steels still grows at the end of the measuring period, it appears to have a saturation limit for static strain aging under certain pre-strain conditions. However, higher pre-strain can result in a higher saturation limit because of larger dislocation density. Moreover, the increasing rate of Vickers hardness for Fe-0.0021C steel is comparable to that of other solute carbon steels at the beginning stage. Therefore, these results suggest that the Fe-0.0021C steel still has relatively stronger DSA capacity compared to IF steel, even though it does not show any serrations arising from DSA in the S-S curve.

2.5 Section conclusion

Based on the tension results at room temperature and static strain aging measurement through Vickers hardness for these five ferritic steels, the DSA hardening in four steels with interstitial carbon content varying from 0.0021% to 0.017% is verified even at room temperature. Moreover, it is evaluated that the tension properties gradually become stronger with the growth of interstitial solute carbon due to both the solid solution hardening and dynamic strain aging hardening.

2.6 Reference

[1] R. Mulford, U. Kocks, New observations on the mechanisms of dynamic strain aging and of jerky flow, Acta Metallurgica, 27 (1979) 1125-1134.

[2] J. Robinson, M. Shaw, Microstructural and mechanical influences on dynamic strain aging phenomena, International Materials Reviews, 39 (1994) 113-122.

[3] A. Van den Beukel, Theory of the effect of dynamic strain aging on mechanical properties, Physica status solidi (a), 30 (1975) 197-206.

[4] A. Van den Beukel, U. Kocks, The strain dependence of static and dynamic strain-aging, Acta Metallurgica, 30 (1982) 1027-1034.

[5] K. Tsuzaki, T. Hori, T. Maki, I. Tamura, Dynamic strain aging during fatigue deformation in type 304 austenitic stainless steel, Materials Science and Engineering, 61 (1983) 247-260.

[6] H. Aboulfadl, J. Deges, P. Choi, D. Raabe, Dynamic strain aging studied at the atomic scale, Acta Materialia, 86 (2015) 34-42.

[7] S. Zhao, C. Meng, F. Mao, W. Hu, G. Gottstein, Influence of severe plastic deformation on dynamic strain aging of ultrafine grained Al–Mg alloys, Acta Materialia, 76 (2014) 54-67.

[8] H.Y. Yasuda, K. Shigeno, T. Nagase, Dynamic strain aging of Al 0.3 CoCrFeNi high entropy alloy single crystals, Scripta Materialia, 108 (2015) 80-83.

[9] D. Wilson, B. Russell, The contribution of atmosphere locking to the strain-ageing of low carbon steels, Acta Metallurgica, 8 (1960) 36-45.

2.7 Figures and tables

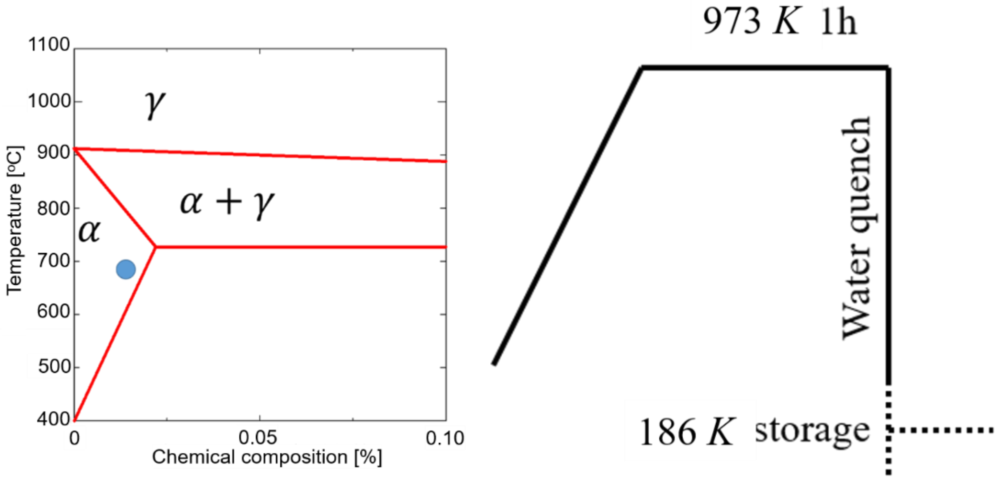

Fig. 2.1. The part iron-carbon phase diagram schematic and corresponding heat treatment

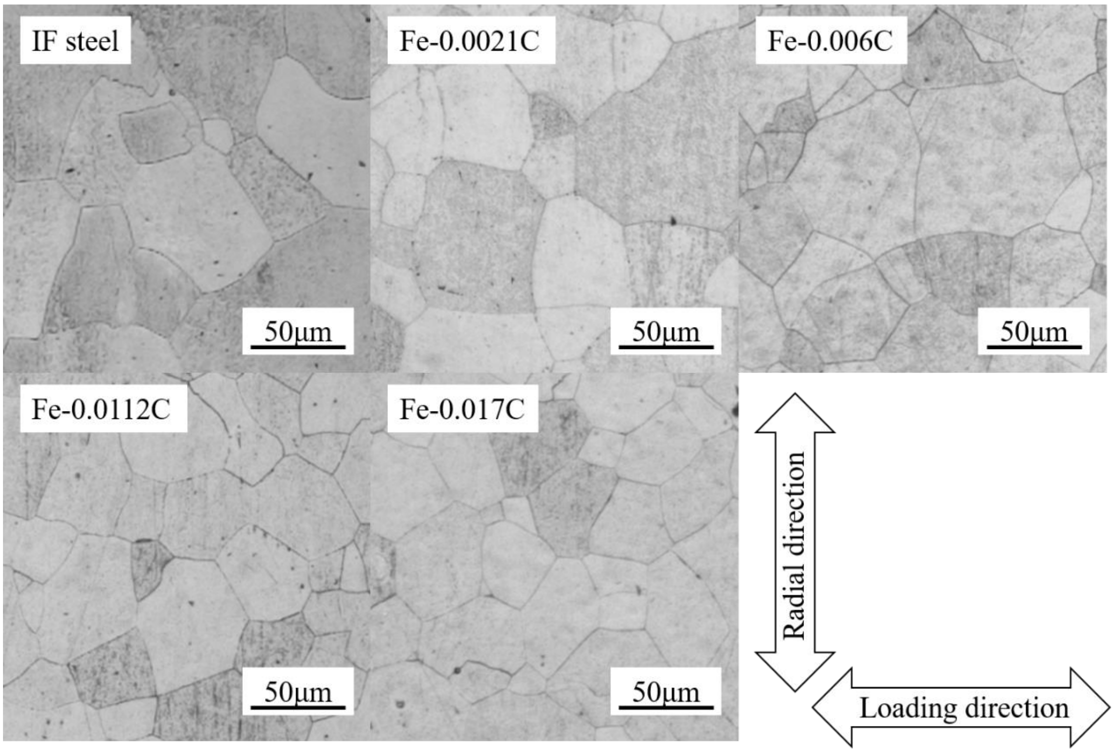

Fig. 2.2. The optical image for microstructure for five ferritic steels

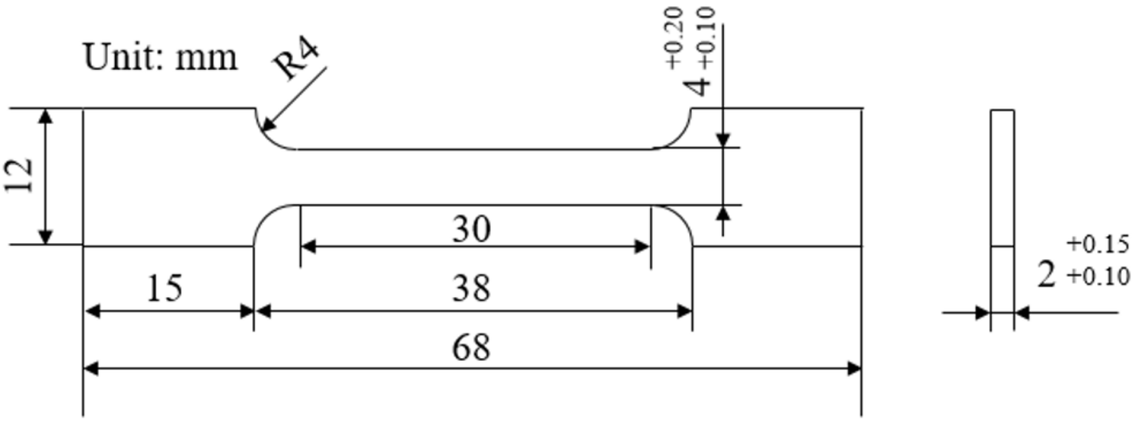

Fig. 2.3. The geometry of tension test specimen

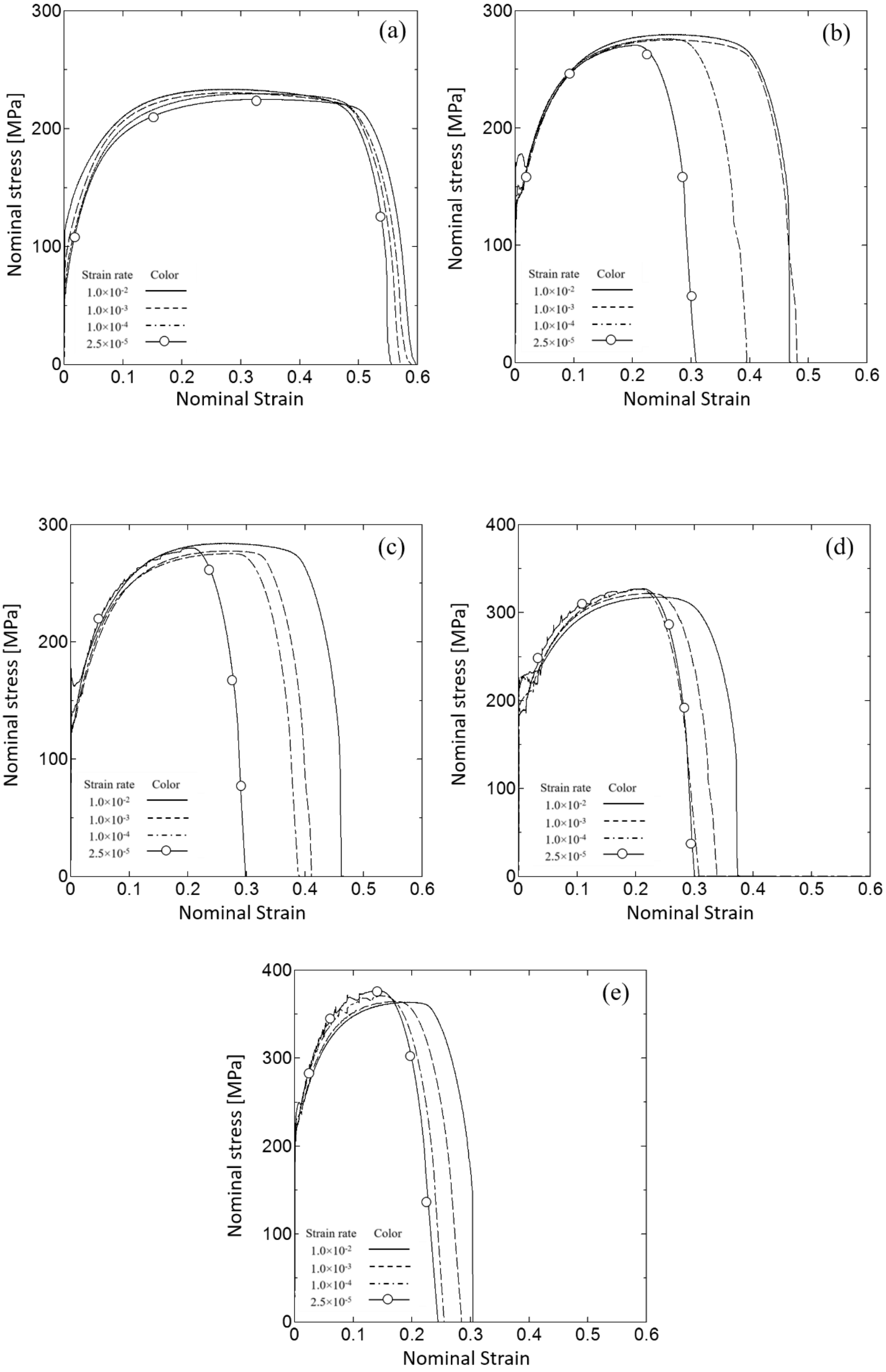

Fig. 2.4 Nominal stress-strain (S-S) curves for the five steels used in this study at different strain rates: (a) IF steel; (b) Fe-0.0021C steel; (c) Fe-0.0063C steel; (d) Fe-0.0112C steel; (e) Fe-0.017C steel.

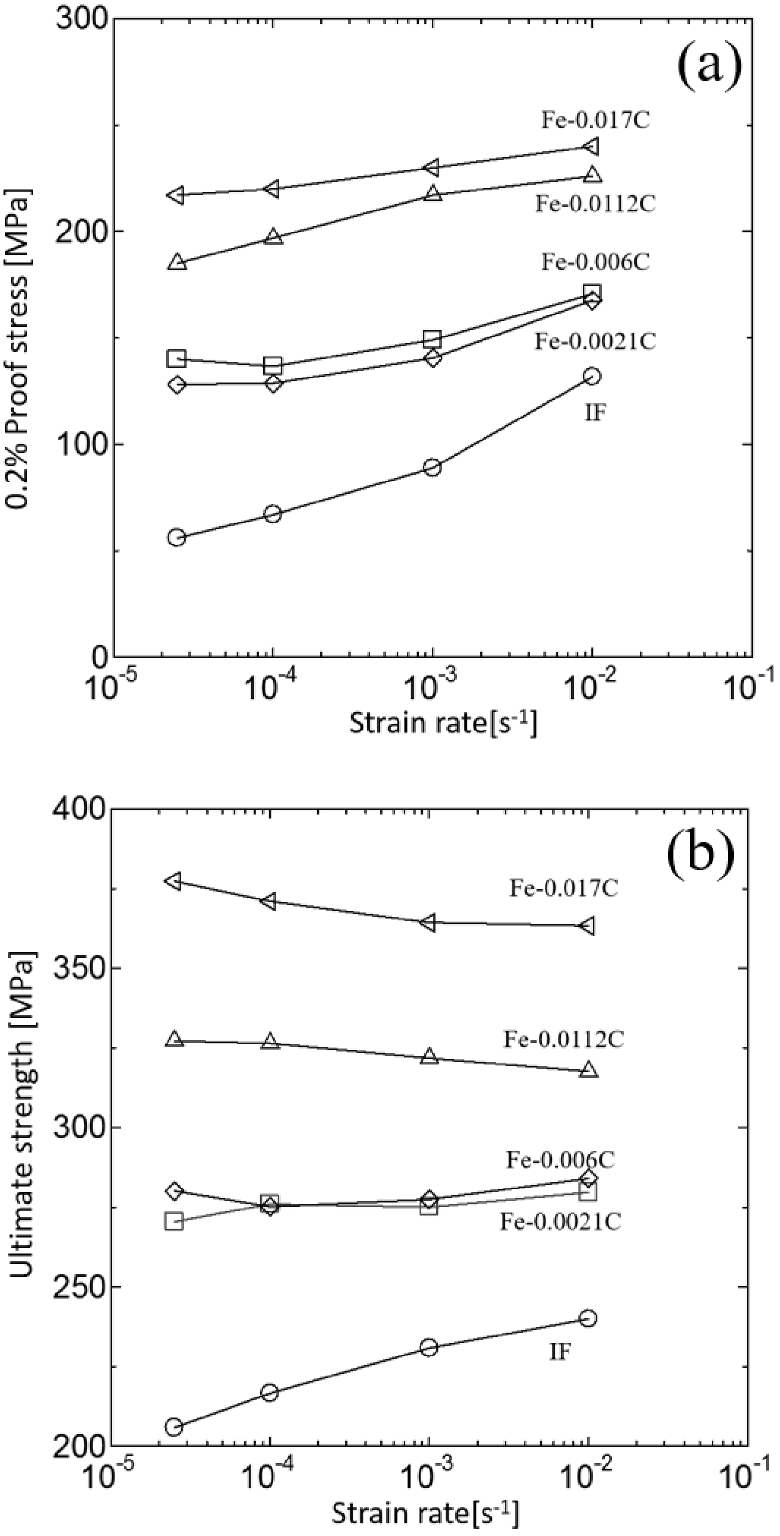

Fig. 2.5 Dependence of the strain rate at (a) 0.2% proof stress and (b) ultimate strength for the five steels used in this study

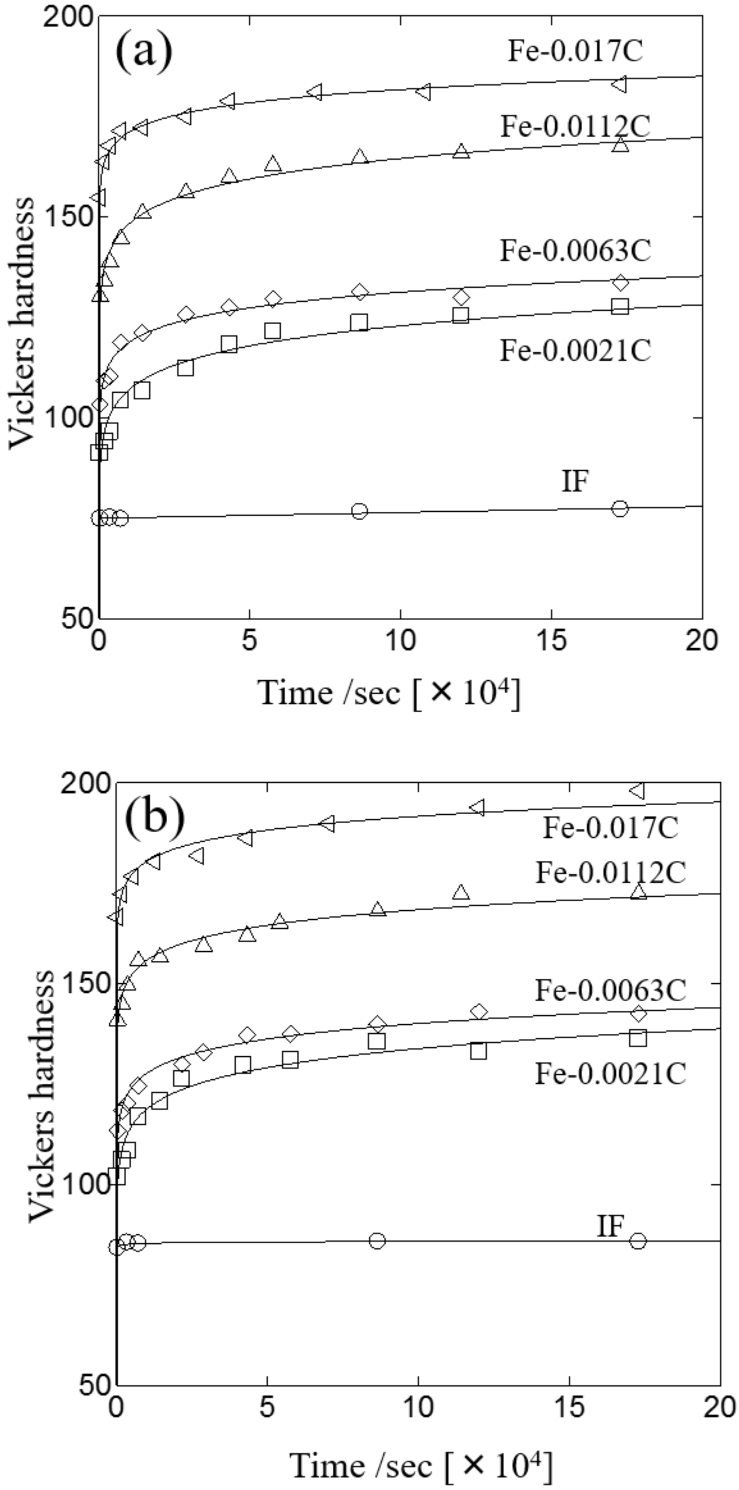

Fig. 2.6 Vickers hardness vs. aging time for the five steels used in this chapter under pre-strain of (a) 4% and (b) 8%

Table 2.1. Chemical composition (wt.%) of the five steels used in this study

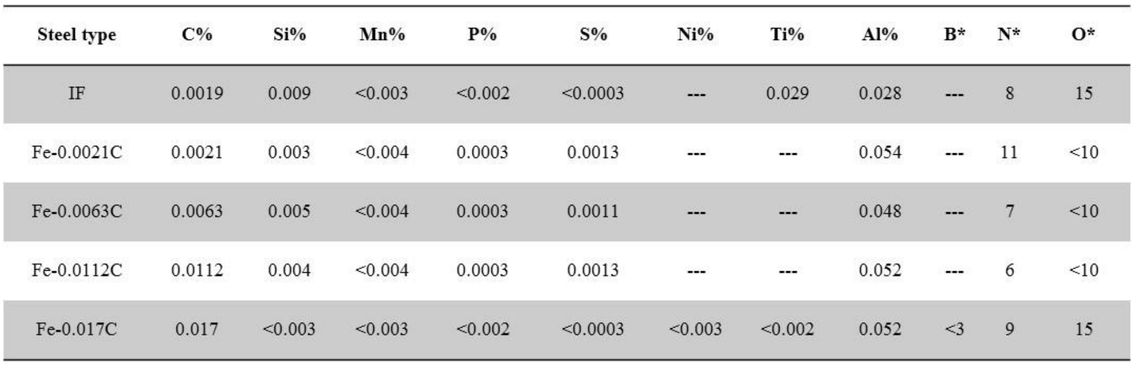

Steel type	C%	Si%	Mn%	P%	S%	Ni%	Ti%	Al%	B*	N*	O*
IF	0.0019	0.009	<0.003	<0.002	<0.0003	---	0.029	0.028	---	8	15
Fe-0.0021C	0.0021	0.003	<0.004	0.0003	0.0013	---	---	0.054	---	11	<10
Fe-0.0063C	0.0063	0.005	<0.004	0.0003	0.0011	---	---	0.048	---	7	<10
Fe-0.0112C	0.0112	0.004	<0.004	0.0003	0.0013	---	---	0.052	---	6	<10
Fe-0.017C	0.017	<0.003	<0.003	<0.002	<0.0003	<0.003	<0.002	0.052	<3	9	15

CHAPTER 3. The evaluation of transgranular fatigue crack resistance for Fe-0.017C alloy with large amount of interstitial carbon at room temperature

3.1 Introduction

Following the tension tests in Chapter 2, the DSA hardening is demonstrated in ferritic steels with interstitial carbon content changing from 0.0021% to 0.017% and is not found in IF steel due to lack of interstitial carbon content. Among these five steels, the Fe-0.017C steel has the largest interstitial carbon concentration and it shows the strongest DSA hardening and solid solution hardening. Therefore, it firstly attracts our attention to investigate its fatigue performance.

In fact, the fatigue test of smooth specimen for Fe-0.017C steel has already been carried out in our previous work [1]. To be exact, the S-N curve of Fe-0.017C steel is totally shown in Fig. 3.1, which reveals the fatigue limit σ_w is around 210 MPa. The main crack initiation characteristic is the intergranular crack initiation and several intergranular cracks coalesce with each other to make crack propagation. Moreover, another characteristic is also observed that not only intergranluar cracking but also transgranular crack occurs at high stress level. However, transgranular crack usually firstly initiates, propagates and finally stops in the grain interior even at high stress level, such as 240 MPa. Based on this observation and phenomenon, it is reasonable to deduce that potential resistance to transgranular fatigue crack propagation in Fe-0.017 is strong and the corresponding fatigue test for Fe-0.017C with micro-notch by using Focus ion beam (FIB) technique is carried out in order to quantify the transgranular fatigue crack resistance. Additionally, the IF steel without any other interstitial solute content is also adopt to compare the result with Fe-0.017C.

3.2 Fatigue experimental procedure

Fatigue tests for these two materials were conducted using an Ono-type rotating bending fatigue testing machine with a stress ratio of -1 and frequency 50Hz in air at room temperature. The specimen shape is shown in Fig. 3.2. Three types of artificial flaws were introduced in the specimen. Type A flaw was introduced using focused ion beam (FIB) milling, and type B and C flaws were introduced using a combination of drilling and FIB. Three flaws were applied for Fe–0.017C alloy, while flaw A and flaw C were applied for IF steel. The corresponding dimensions of these flaws are also described in Fig. 3.2. The fatigue crack growth was examined using the replica method with an optical microscope.

3.3 Capability of Murakami equation and definition of $\sqrt{area}$ for irregular flaw

In order to estimate the growth degree of the threshold stress intensity factor range ΔK_{th} of Fe-0.017C alloy and IF steel, Murakami’s equation, which only requires the

Vickers hardness Hv and $\sqrt{area}$ of the flaw to predict the small notch or crack threshold, was used as the reference standard [2]:

$$\Delta K_{th} = 0.65\Delta\sigma_w\sqrt{\pi\sqrt{area}} \tag{3.1}$$

$$\Delta K_{th\_pre} = 3.3 \times 10^{-3}(Hv + 120)(\sqrt{area})^{1/3} \tag{3.2}$$

$$I\% = \frac{\Delta K_{th} - \Delta K_{th\_pre}}{\Delta K_{th\_pre}} \times 100\% \tag{3.3}$$

where $\Delta\sigma_w$ and $\sqrt{area}$ are the non-propagating fatigue limit and the square root of the area obtained by projecting the flaw onto a plane perpendicular to the loading axis direction, respectively. $\Delta K_{\mathrm{th\_pre}}$ is the predicted fatigue threshold, and I is the predicted deviation of the experimental result from the predicted result.

In fact, Murakami's equation can not only be used to predict the internal crack initiation by inclusion, but also be used to predict the small crack propagation threshold for various materials, especially for carbon steel. The capability of its prediction accuracy is shown in Fig. 3.4(a), almost all the experimental data from various materials with different geometrically initial notches or holes fall within the 10% error interval band at least for carbon steel. Therefore, it is reasonable to regard this equation as a reference standard to reflect the influence of considerable interstitial carbon concentration in ferritic steel.

In addition, in terms of irregular shape flaw such as type B and type C flaws, the definition of $\sqrt{area}$ should be clear. The finite element analysis of type B and C is described in Fig. 3.3(a) and Fig. 3.3(b) is the corresponding schematic. It can be seen from Fig. 3.3(b) that point A and point E have the maximum stress concentration meaning that crack will initiate from these both points and be inclined to become smoothly contoured crack after propagation and subsequent non-propagation [3]. Hence, the definition of $\sqrt{area}$ for irregular shape flaw in this paper is the contour DBCIGFHD in Fig. 3.3(b), which is similar with that in [4].

3.4 Experimental results and analysis

The experimental data for the Fe-0.017C alloy and IF steel are shown in Fig. 3.4(b). In the IF steel, the threshold values with different initial notch sizes are obtained as exhibited in Table 3.1 and the corresponding replica images are described in Figs. 3.5(a-c). The threshold value increases with the increase of initial notch or crack size due to different saturation opening stress intensity factor K_{op}. More specifically, the relevant threshold values for types A and C flaws are 2.55 and 3.75 MPa$\sqrt{m}$, respectively. It is noticeable that the prediction errors in the IF steel with different notch shapes and sizes are both less than -10%, which once again verifies the effectiveness of Murakami's equation for general ferritic steels.

Next, note the fatigue test results of the Fe-0.017C alloy. As shown in Fig. 3.4(b) and Figs. 3.5(d-f), the specimens with types A or B flaws did not fracture even when the stress amplitude was increased to 210 MPa which was the fatigue limit of the smooth specimen [1]. Fig. 3.5(g) shows a crack initiating from a grain boundary at 210 MPa in the specimen with the non-propagating fatigue crack. This crack along the grain boundary was far away from the notch tip. This fact implies that this notched specimen would fracture due to the intergranular crack initiation and propagation, which is the same failure mechanism of the smooth specimen [1]. In other words, the stress concentration at the notch tip cannot be a cause of failure, even if the stress level is more than 210 MPa. The threshold value of the Fe-0.017C alloy was finally determined to be 7.93 MPa$\sqrt{m}$ when the initial crack size $\sqrt{area}$ was increased to 337 μm, which is about 40.5% higher compared with the Murakami's equation-based prediction.

As can be seen from Fig. 3.5, all of the fatigue cracks for both materials firstly propagate to grain interior when the crack is near the notch tip because of the influence of notch geometry. To be exact, the surface crack does not propagate along grain boundaries even when meeting a grain boundary because the propagation direction is three-dimensionally confined by not only the specimen surface geometry but also the geometry along the specimen depth direction (normal of the specimen surface), as illustrated in Fig. 3.6 which reveals the SEM fractograph of specimen E in Fig. 3.4(b). The fracture surface was obtained by fatigue testing and subsequent fracture at 77 K. The non-propagating crack zone with the artificial flaw is contoured by dotted line, obviously showing no intergranular propagation feature. In contrast, when the fatigue crack becomes long, it prefers to propagate intergranularly as shown in Fig. 3.5(c) and Fig. 3.5(f), which is similar to the behavior of the smooth specimen [1]. The intergranular propagation behavior of the long cracks is more distinct in the IF steel. This behavior is a quite important aspect of the water quenched Fe-0.017C alloy. Specifically, the water quenching is considered to suppress carbon segregation on grain boundary, and thus the interstitial carbon content in the grain interior is as high as possible in the Fe-0.017C alloy. With respect to the non-propagating specimen, the non-propagating crack is short enough, hence, it is reasonable to believe that dynamic strain aging (DSA) can contribute to its stopping. Specifically, Fig. 3.7 depicts the fatigue crack growth curve of Flaw C for both materials. Generally, at the initial stage of crack propagation for fracture specimen, the effective stress intensity factor range ΔKeff firstly decreases with crack growth, arrives at one minimum value and finally increases with crack growth mainly because of crack closure influence [5]. If this minimum value is lower than effective threshold $\Delta K_{\mathrm{effth}}$, the crack becomes non-propagating, e.g. as shown in Fig. 3.7. According to the plastic-induced crack closure (PICC) model [6], higher yield strength can result in more significant PICC influence for small crack, namely higher ΔK_{th}. As DSA can contribute to increase of yield strength with time, it is rational to deduce that one of mechanisms for impeding crack due to DSA is the growth of crack closure effect.

Murakami's equation is a very effective threshold prediction method, which only needs two parameters Hv and $\sqrt{area}$. However, only influences of notch or crack size and static mechanical property are considered in the equation. In other word, the equation does not include the kinetic effects such as strain-age hardening. In fact, the kinetic effect leads to a large predicted deviation as calculated in Table 3.1. Thus, the strain–age hardening during fatigue testing is considered as the primary factor increasing ΔK_{th} in the Fe-0.017C alloy.

3.5 Section conclusion

The influences of considerable interstitial carbon concentration and associated strain aging on threshold value of fatigue crack growth, ΔK_{th}, were investigated by using the Fe–0.017C (wt%) alloy and interstitial-free steel. Two kinds of flaws with different shapes and sizes were used to demonstrate that the Fe–0.017C alloy threshold value is always much higher than that of IF steel. The threshold value ΔK_{th} of the Fe-0.017C alloy with an artificial flaw was approximately 40.5% higher than Murakami's equation-based prediction. This fact was explained by the strengthening effect associated with the diffusion kinetics of carbon, i.e., the effect of strain aging during the fatigue test. This finding suggests that ferritic steels have the potential to attain greater fatigue resistance via the increase of the solute carbon content, particularly in practical structures with a considerable amount of scratches and inclusions.

3.6 Reference

[1] M. Koyama, Z.-J. Xi, Y. Yoshida, N. Yoshimura, K. Ushioda, H. Noguchi, Intergranular fatigue crack initiation and its associated small fatigue crack propagation in water-quenched Fe–C fully ferritic steel, ISIJ International, 55 (2015) 2463-2468.

[2] Y. Murakami, Metal fatigue: effects of small defects and nonmetallic inclusions: effects of small defects and nonmetallic inclusions, Elsevier, 2002.

[3] M. Yukitaka, E. Masahiro, Quantitative evaluation of fatigue strength of metals containing various small defects or cracks, Engineering Fracture Mechanics, 17 (1983) 1-15.

[4] Y. Murakami, H. Matsunaga, A. Abyazi, Y. Fukushima, Defect size dependence on threshold stress intensity for high‐strength steel with internal hydrogen, Fatigue & Fracture of Engineering Materials & Structures, 36 (2013) 836-850.

[5] S. Suresh, Fatigue of materials, Cambridge university press, 1998.

[6] N. Fukumura, T. Suzuki, S. Hamada, K. Tsuzaki, H. Noguchi, Mechanical examination of crack length dependency and material dependency on threshold stress intensity factor range with Dugdale model, Engineering Fracture Mechanics, 135 (2015) 168-186.

3.7 Figures and tables

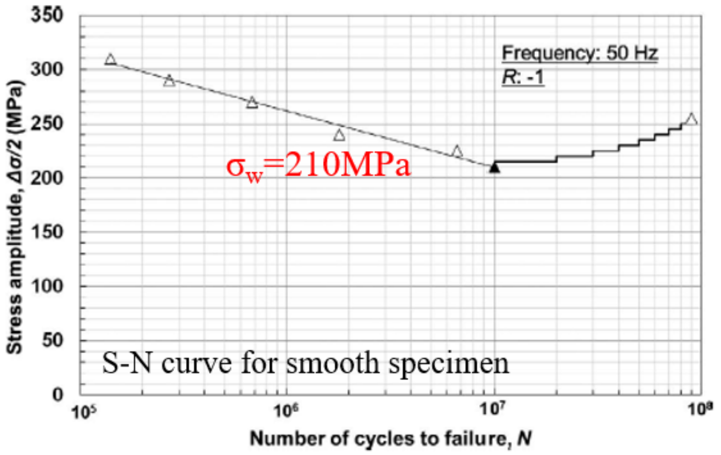

Fig. 3.1 The S-N curve for smooth specimen of Fe-0.017C at room temperature [1]

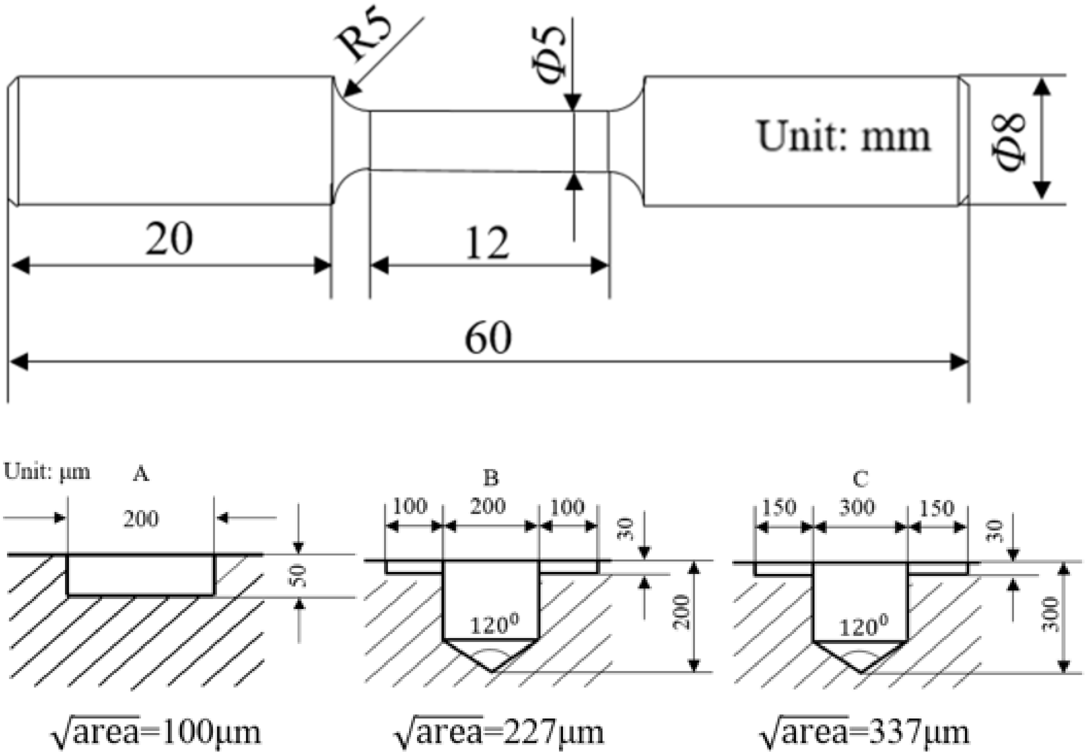

Fig. 3.2 The geometry of the fatigue test specimen with three kinds of micro-notches

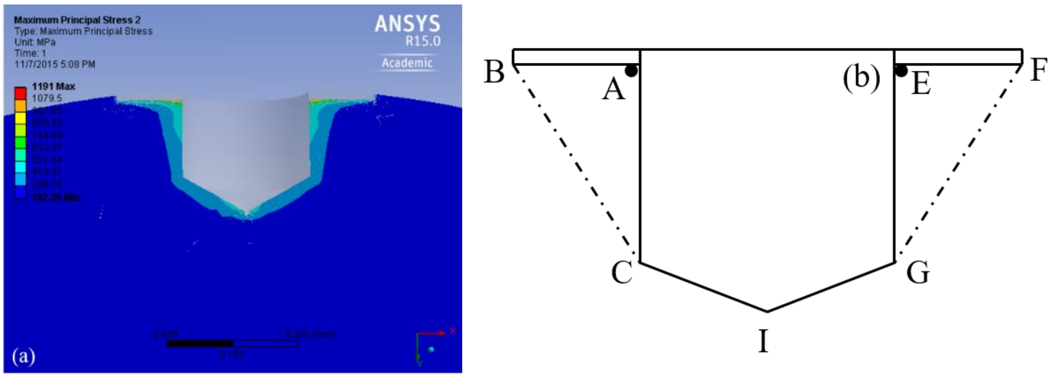

Fig. 3.3 Irregularly shape flaws: (a) stress analysis; (b) the effectively estimated $\sqrt{area}$

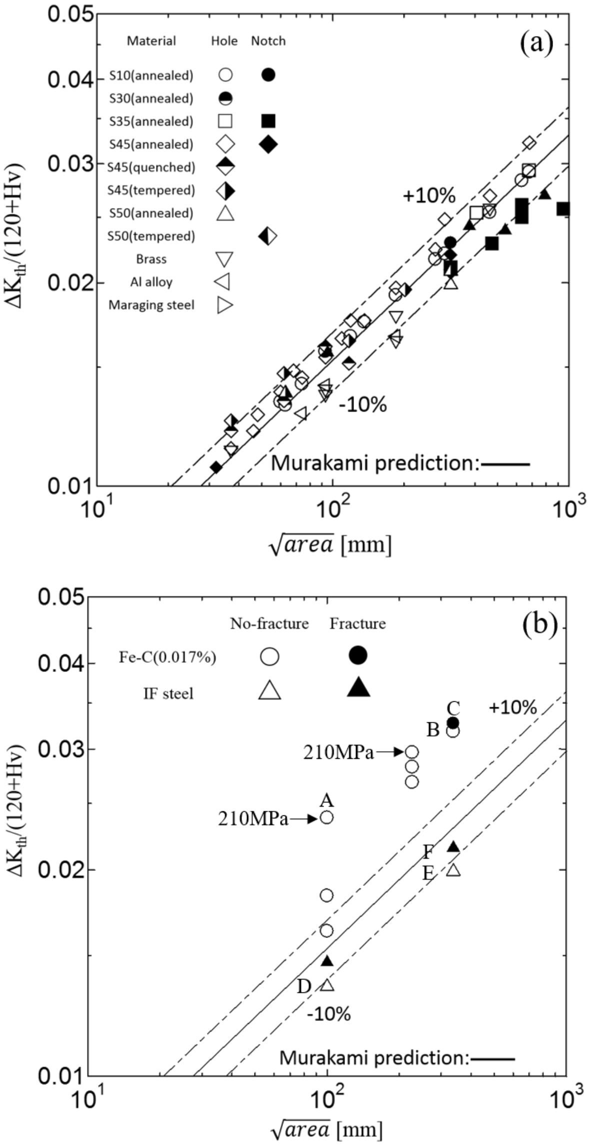

Fig. 3.4 Murakami equation prediction: (a) prediction capability for conventional steel (b) prediction result for Fe-C alloy (0.017% w.t) and IF steel

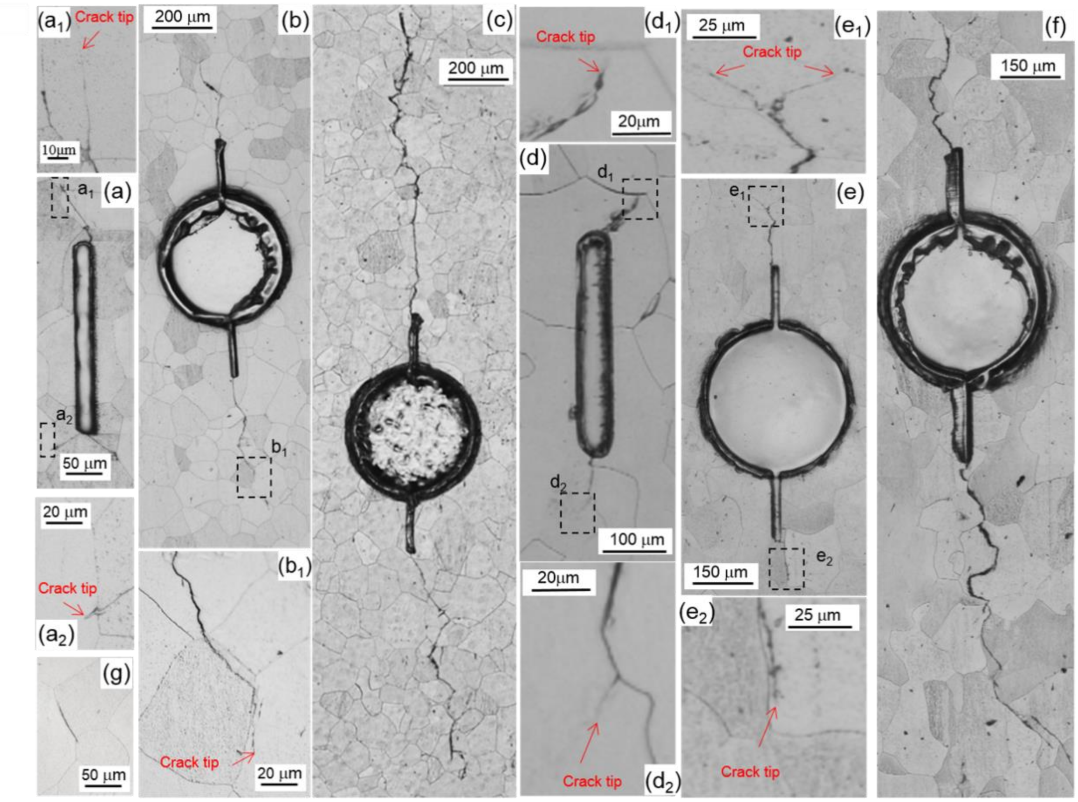

Fig. 3.5 Optical micrographs of non-propagating specimen and fracture specimen on Fe-C alloy and IF steel in Fig. 3.4(b): (a) specimen A; (b) specimen B; (c) specimen C; (d) specimen D; (e) specimen E; (f) specimen F; (g) Crack initiation at grain boundary under 210MPa for non-propagating specimen of Fe-C alloy

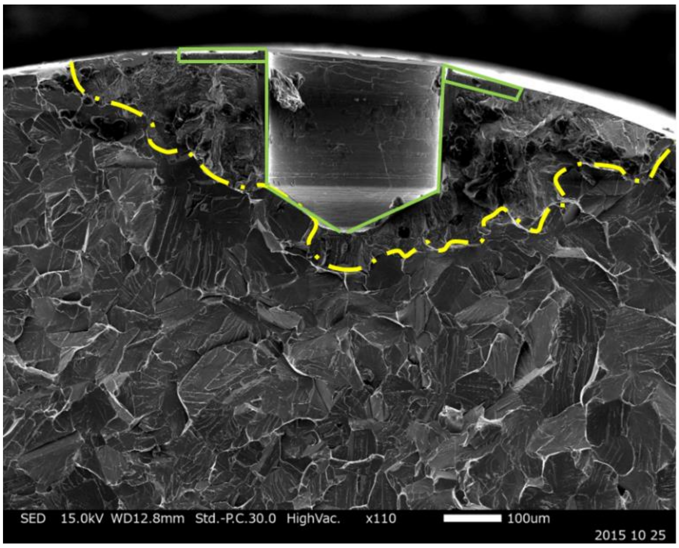

Fig. 3.6 SEM image of specimen B in Fig. 3.4(b) by using brittle fracture at low temperature in liquid nitrogen

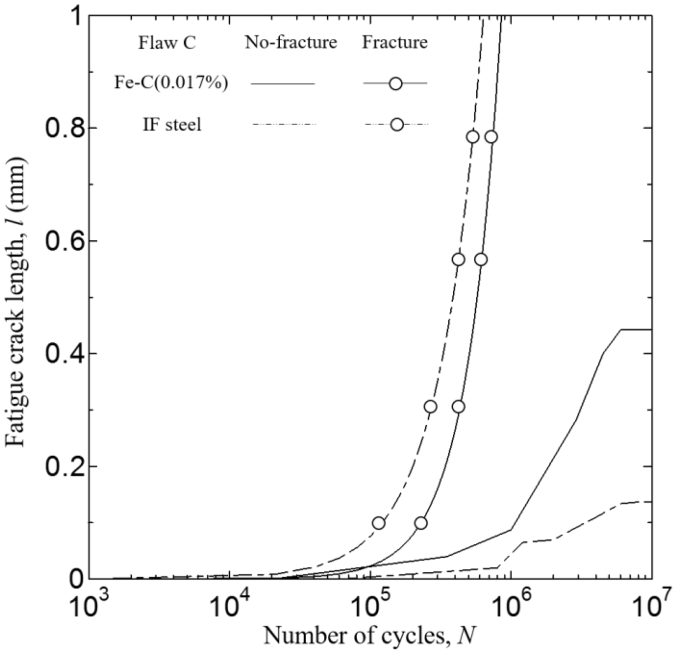

Fig. 3.7 Crack growth length curve for both materials with Flaw C

Table 3.1. Predicted and experimental results of two materials

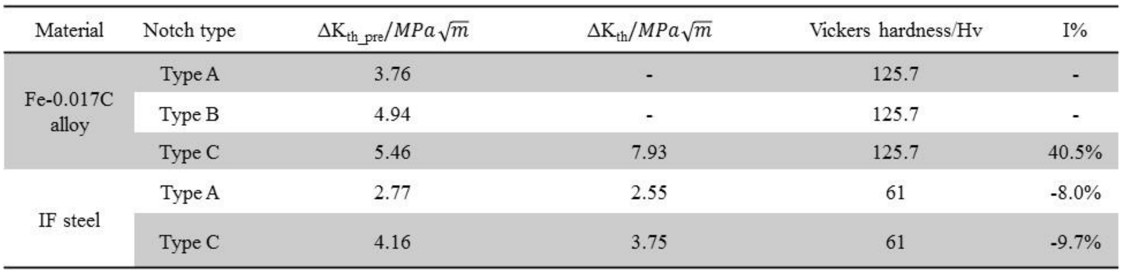

Material	Notch type	$\Delta K_{th\_pre}/MPa\sqrt{m}$	$\Delta K_{th}/MPa\sqrt{m}$	Vickers hardness/Hv	I%
Fe-0.017C alloy	Type A	3.76	-	125.7	-
	Type B	4.94	-	125.7	-
	Type C	5.46	7.93	125.7	40.5%
IF steel	Type A	2.77	2.55	61	-8.0%
	Type C	4.16	3.75	61	-9.7%

CHAPTER 4. Interstitial carbon concentration dependence of transgranular fatigue crack resistance for five ferritic steels at room temperature

4.1 Introduction

Obviously, significant potential resistance to transgranular fatigue crack is found in Fe-0.017C with single ferrite phase in Chapter 3, whose experimental value is around 40% higher than that of prediction value by Murakami equation. The remarkable potential resistance presumably results from DSA hardening. However, the Chapter 3 only reveals the difference on transgranular fatigue crack resistance between IF without any solute carbon and Fe-0.017C within largest amount of interstitial carbon in five ferritic steels. In order to further investigate the solute carbon concentration dependence of transgranular fatigue crack resistance, fatigue tests of additional three ferrtic steels with different solute carbon contents are conducted and the mechanism of solute carbon concentration to transgranular fatigue crack resistance was analyzed in this chapter in detail.

4.2 Fatigue experimental procedure

The fatigue test for the additional three ferritic steels is also carried out in Ono-type rotating bending fatigue testing machine which is totally same as that in Chapter 3. It should be noticed that the specimen shape is same as shown in Fig. 3.2, however, only type C notch with crack size 337 μm is employed in this Chapter 3. SEM and optical microscope are used to capture the information for crack initiation and propagation behavior.

4.3 Experimental results and discussion

4.3.1 The existence of dynamic strain aging under cyclic loading at room temperature

The fatigue experimental data for all the steels are shown in Fig. 4.1 and Table 4.1 in detail. The corresponding Vickers hardness values measured before fatigue testing are depicted in Fig. 4.2. The relationship between the Vickers hardness and normalized carbon content tend to be linear due to the solid solution. In the IF steel and Fe-0.017C steel, the relevant threshold values ΔK_{th} are 3.75 MPa$\sqrt{m}$ and 7.93 MPa$\sqrt{m}$, respectively, which have already been determined in Chapter 3 or in our published work [1]. In the case of Fe-0.0021C steel, the threshold value ΔK_{th} is 5.38 MPa$\sqrt{m}$ which is around 43.4% and 21.6% higher than the value of IF steel and the predicted value by Murakami's equation, respectively. According to Murakami equation in Eq. (3.2), the threshold value ΔK_{th} increases with the increase of Vickers hardness and the crack size. Hence, a large difference of threshold values between Fe-0.0021C steel and IF steel in Fig. 4.1a is partly because of the variance of initial Vickers hardness before fatigue test due to different extent of solid solution hardening. Continuously increasing the carbon concentrations can lead to the further growth of threshold value as depicted in Fig. 4.1a and in Table 4.1 for steels with higher carbon concentrations. More specifically, the threshold values of Fe-0.0063C and Fe-0.0112C steels are 5.94 MPa$\sqrt{m}$ and 6.94 MPa$\sqrt{m}$, respectively. Distinctly, the growth of threshold value from carbon content 0.0021% to 0.0063% is approximately 0.56 MPa$\sqrt{m}$, while the value is 1.63 MPa$\sqrt{m}$ with carbon concentration varying from 0 to 0.0021%. That is to say, the contribution of increased carbon content in Fe-0.0063C steel compared with Fe-0.0021C steel to threshold value enhancement is much less than that in Fe-0.0021C steel compared with IF steel. Similar result can also be observed in higher carbon content steels. However, normalized ΔK_{th} shown in Fig. 4.1b whose tendency excludes the effect of hardness also shows distinct increases against solute carbon content. More specifically, the corresponding variation tendency of ΔK_{th} with carbon content shows two distinct growth slopes, k_1 and k_2, exists. To discuss reasons for the slopes k_1 and k_2, further mechanisms must be considered in terms of roles of solute carbon on strengthening at a crack tip.

The replica images of specimens with non-propagating crack and fractured specimens for five steels are described in Figs. 4.3 and 4.4, respectively. It can be seen evidently from Fig. 4.3 that fatigue cracks always initiate at the FIB-notch tip due to the stress concentration and then propagate in the grain interior. When the fatigue crack arrives at the GB, in most cases, the fatigue crack can propagate across the GB rather than along the GB due to the influence of three-dimensional geometries of initial notch geometry and subsequently formed crack tip. Although the non-propagating crack of Fe-0.017C steel shown in Fig. 4.3e sometimes grows along the GB, the transgranular propagation feature has already been verified to be major by using SEM image of fracture surface [1]. Moreover, all the non-propagating cracks finally stop in the grain interior rather than GB. Actually, a major amount of solute carbon atoms exists in grain interior in the as-water-quenched condition because of lack of diffusion time for carbon segregation to GB and prominent DSA ability is expected for transgranular non-propagation crack which results in threshold value enhancement. Hence, below the experimentally determined ΔK_{th}, a primary factor triggering fatigue crack non-propagation is transgranular crack growth behavior, irrespective of carbon content.

In the light of fractured specimen described in Fig. 4.4, transgranular propagation behavior also occurs when the fatigue crack length is short enough, which is same as specimen with non-propagating crack, while intergranular propagation behavior appears when the fatigue crack is long enough where the influence of initial notch geometry become less and this propagation behavior is more distinct in IF steel and Fe-0.0021C steel. This characteristic phenomenon about the transition of propagation behavior from transgranular to intergranular manners seems to be another key factor to enhance the $\Delta \mathrm{K}_{th}$ for solute carbon steels. Specifically, cohesive strength of GB in the IF and 0.0021C steels affects resistance to crack propagation above the $\Delta \mathrm{K}_{th}$, which may cause a lower $\Delta \mathrm{K}_{th}$ than ideal $\Delta \mathrm{K}_{th}$. In addition to the effect of DSA on transgranular crack growth, an influence of cohesive strength of GB is discussed in the next section.

4.3.2 The analysis about the influence of solute carbon content on ΔK_{th}

As discussed above with Fig. 2.6, the Vickers hardness or yield stress after plastic straining increases with aging time because of strain-age hardening. Likewise, plastic zone exists in front of crack tip under cyclic loading and much more dislocations can be generated in this zone. In fact, the dislocation structure in front of fatigue crack tip in ferrite phase has been investigated by previous studies [2, 3]. Zheng et al. [3] studied the dislocation structure in front of short crack tip on the near-threshold condition in a dual-phase ferrite-martensite steel and found that dislocation cell and wall structures formed in ferrite phase. As well, Huang et al [2] also made similar conclusion by using Fe-Al-Mn-0.4%C steel under near-threshold condition. As the cell wall and wall structures are the dense dislocation region in microstructure which can be regarded as the obstacle for mobile dislocation motion, the new mobile dislocation emitted from fatigue crack tip can be blocked and make shuttling motion in dislocation cell. In cell-shuttling motion, mobile dislocation can rapidly glide between the cell walls and pile up on the cell wall [4]. DSA during the fatigue testing may occur because of arrest time of dislocations at the obstacles such as cell walls in the high plastic strain zone at a crack tip. As a result of the DSA, yield strength in front of the crack tip is increased. Meanwhile, the yield strain in front of the crack tip is a crucial parameter to control the effect of plasticity-induced crack closure (PICC) for small crack and higher yield strain can result in higher ΔK_{th} value [5]. Consequently, the improvement of PICC capacity is one of the mechanisms to increase the ΔK_{th} because of DSA, and it is reasonable to believe that the significant improvement of ΔK_{th} with the steep slope of k_1 in Fig. 4.1b by increasing carbon content from 0 to 0.0021% is owing to the DSA even if any serrations arising from DSA does not appear on S-S curves of the Fe-0.0021C steel.

In the second place, the fracture surfaces of the five steels shown in Fig. 4.5 demonstrate two conspicuous characteristics. One of them is the transgranular propagation feature around the crack initiation area which is shown in the replica images of Figs. 4.3 and 4.4, whilst another characteristic is the gradual disappearance of intergranular cracking feature with increasing carbon content in fracture surface and the corresponding zone is magnified in the corner of each pictures with dotted line as depicted in Fig. 4.5. To be exact, the fracture surface can be divided into three parts as shown in Fig. 4.5(f). Part A is the area around the micro-notch, Part B corresponds to fast propagation region which is not affected by initial notch geometry, and Part C is the final fracture region. For IF steel and Fe-0.0021C steel, because of a poor amount of solute carbon, the GB cohesive strength is much lesser and a remarkable intergranular cracking occurs in Part B, which is similar behavior with the crack initiation and propagation in smooth specimen of IF steel [6, 7]. The percentage of intergranular cracking feature in Part B decreases for higher solute carbon steel (from 0.0063% to 0.017%) and no intergranular feature is observed in fracture surface of Fe-0.017C steel. In other words, the cohesive strength of GB is improved with increase of carbon concentration due to different extent of uncontrolled carbon segregation to GB. These facts indicate that the enhancement of cohesive strength of GB by carbon becomes gradually remarkable when the carbon content is higher than 0.0021%. Thanks to the carbon segregation, not only cohesive strength of GB but also the ability of GB to impede the dislocation motion increases [8]. Namely, more dislocations can be piled up against GB before new dislocation can emit from the GB with increase of carbon content. As the non-propagating crack more or less propagates across several GBs as shown in Fig. 4.4, the effect of dislocation pile at the carbon-strengthened GB also must contribute to ΔK_{th} improvement. Hence, the effects of solute carbon on cohesive strength of GB and dislocation pile-up at the carbon-decorated GB on fatigue crack growth gradually acts particularly at higher carbon content. This phenomenon is one of the reasons why the moderate slope of k_2 appeared at the carbon content region ranging from 0.0063% to 0.017%.

Additionally, the intergranular crack initiation mechanism of water-quenched steel (i.e. Fe-0.017C steel) should be considered further as revealed in Fig. 4.6. It should be noticed here that the replica images in Fig. 4.6 is taken from the specimen of Fe-0.017C steels with only one FIB-notch at 210 MPa [1], which is the fatigue limit of plain specimen [9]. The location of the fatigue crack in Fig. 4.6 is far away from the FIB-notch tip position, therefore, its crack initiation mechanism is not because of FIB-notch stress concentration but same as that in smooth specimen. It can be seen clearly from Fig. 4.6 that a micro-crack firstly appears at the vicinity of GB colored by blue dotted line when the number of fatigue cycles reaches 1.2×10^5. Here note that the fatigue crack is initiated near GB, not on GB. Then several micro-cracks generate in the following cycles and coalesce with each other, which increases the crack length. Based on above observation, it is evident to know that the area at the vicinity of GB is the weakest zone called as solute poor zone in this paper. The weakness of locations near GB is presumably because of presence of solute poor zone near GB that formed during sample preparation and fatigue testing due to uncontrolled carbon segregation to GB. Although the intergranular cracking in the IF steel is discussed with cohesive strength of GB, the intergranular cracking in the 0.017C steel is considered to be dominated by local resistance to plastic deformation because the cohesive strength of GB is sufficiently enhanced by carbon. Specifically, the relative resistance to plastic deformation in the solute poor zone is a primary factor causing the intergranular cracking in the Fe-0.017C steel. This consideration can be deepened by the comparison about coaxing effect for plain specimen among three materials (IF, Fe-0.0063C and Fe-0.017C steel) [10]. In terms of the coaxing effect of Fe-0.017C steel, it has more than 9 increment steps and no new intergranular cracking occurs during the coaxing test before fracture, whereas Fe-0.0063C steel showed failure after only three increment steps. Namely, new intergranular crack initiation is suppressed by coaxing effect. As micro-crack formation at the vicinity of GB is the cause of intergranular cracking, it can deduce that large difference exists in solute poor zone between Fe-0.0063C and Fe-0.017C steels in terms of DSA influence. In other word, resistance to plastic deformation in solute poor zone can be improved by the DSA, whose effect on fatigue crack growth is enhanced with the increase of carbon content.

The mechanism of transgranular fatigue crack propagating through GB in the Fe-0.017C steel is investigated as shown in Fig. 4.7. The fatigue crack is arrested firstly when it meets the GB also colored by blue dotted line. Due to stress concentration and subsequent plasticity accommodation in front of crack tip, micro-crack is generated near the other side of GB. With the damage accumulation, eventually, main crack coalesces with the newly formed micro-crack and successfully propagates through GB. However, after some extent of crack growth, it finally stops in the grain interior due to DSA effect. Assuming that solute poor zone is also present near the GB, this phenomenon indicates that both the strength and DSA capacity in solute poor zone can have quite a few influence on ΔK_{th} value. Namely, it is considered that the slope k_2 appearing in the high carbon concentration region in Fig. 4.1b is attributed to the two factors at least: 1) improvement of GB cohesive strength and ability to impede dislocation motion; 2) the enhancement of strength and DSA capacity of the solute poor zone.

Lastly, the schematic illustration about the difference among five materials in terms of the solute content effect is described in Fig. 4.8. In the case of IF steel, as no solute carbon atom exists, there is no DSA effect further improving the yield strength in front of crack tip and weakest GB resistance to transgranular fatigue crack. With the rise of carbon content, such as Fe-0.0021C steel, almost all carbon atoms are located in grain interior rather than on GB. Because of influence of dislocation structure ahead of crack tip, dislocation motion emitted from crack tip is confined in substructure (e.g. dislocation cell) and easier to be locked by solute atom. Nevertheless, due to extra-low carbon concentration, GB resistance to fatigue crack cannot be enhanced to some extent and solute poor zone exists near the GB due to uncontrolled carbon segregation. That is to say, larger growth slope k_1 in Fig. 4.1b entirely results from the DSA effect in grain interior. Further increase of carbon content actually has lesser extra advancement of

DSA effect in grain interior as strain aging capacity has its saturation limit, while it can lead to larger extent of carbon segregation to GB which advances the GB resistance to fatigue crack and GB cohesive strength for intergranular cracking. Meanwhile, the strength and DSA influence in solute poor zone can also be strengthened gradually. Therefore, increasingly stronger GB and solute poor zone contribute to the smaller growth slope k_2 in Fig. 4.1b.

4.4 Section conclusion

The threshold value of small crack under cyclic loading for five materials is determined, which firstly increases significantly and then enhances slowly with the growth of carbon content. The first larger growth slope k_1 stems from the enhanced DSA effect in grain interior and the second smaller growth slope k_2 results from the improved strength and resistance of GB and advanced strength and DSA effect in solute poor zone at the vicinity of GB.

4.5 Reference

[1] B. Li, M. Koyama, E. Sakurada, N. Yoshimura, K. Ushioda, H. Noguchi, Potential resistance to transgranular fatigue crack growth of Fe–C alloy with a supersaturated carbon clarified through FIB micro-notching technique, International Journal of Fatigue, 87 (2016) 1-5.

[2] H. Huang, N. Ho, The microstructure of the fatigue crack tip in Fe–Al–Mn–0.4% C alloy near the stress intensity threshold, Materials Science and Engineering: A, 293 (2000) 235-241.

[3] Y. Zheng, Z. Wang, S. Ai, Effect of dislocation substructure of crack tip on near fatigue threshold in dual-phase steels, Materials Science and Engineering: A, 176 (1994) 393-396.

[4] K. Tsuzaki, Y. Matsuzaki, T. Maki, I. Tamura, Fatigue deformation accompanying dynamic strain aging in a pearlitic eutectoid steel, Materials Science and Engineering: A, 142 (1991) 63-70.

[5] N. Fukumura, T. Suzuki, S. Hamada, K. Tsuzaki, H. Noguchi, Mechanical examination of crack length dependency and material dependency on threshold stress intensity factor range with Dugdale model, Engineering Fracture Mechanics, 135 (2015) 168-186.

[6] S. Majumdar, D. Bhattacharjee, K. Ray, Mechanism of fatigue failure in interstitial-free and interstitial-free high-strength steel sheets, Scripta Materialia, 64 (2011) 288-291.

[7] N. Narasaiah, P. Chakraborti, R. Maiti, K. Ray, Fatigue crack initiation in an interstitial free steel, ISIJ international, 45 (2005) 127-132.

[8] S. Takaki, D. Akama, N. Nakada, T. Tsuchiyama, Effect of Grain Boundary Segregation of Interstitial Elements on Hall–Petch Coefficient in Steels, Materials Transactions, 55 (2014) 28-34.

[9] M. Koyama, Z.-J. Xi, Y. Yoshida, N. Yoshimura, K. Ushioda, H. Noguchi, Intergranular fatigue crack initiation and its associated small fatigue crack propagation in water-quenched Fe–C fully ferritic steel, ISIJ International, 55 (2015) 2463-2468.

[10] M. Koyama, B. Ren, N. Yoshimura, E. Sakurada, K. Ushioda, H. Noguchi, Intrinsic Factors that Trigger the Coaxing Effect in Binary Fe–C Ferritic Alloys with a Focus on Strain Aging, ISIJ International, 57 (2017) 358-364.

4.6 Figures and tables

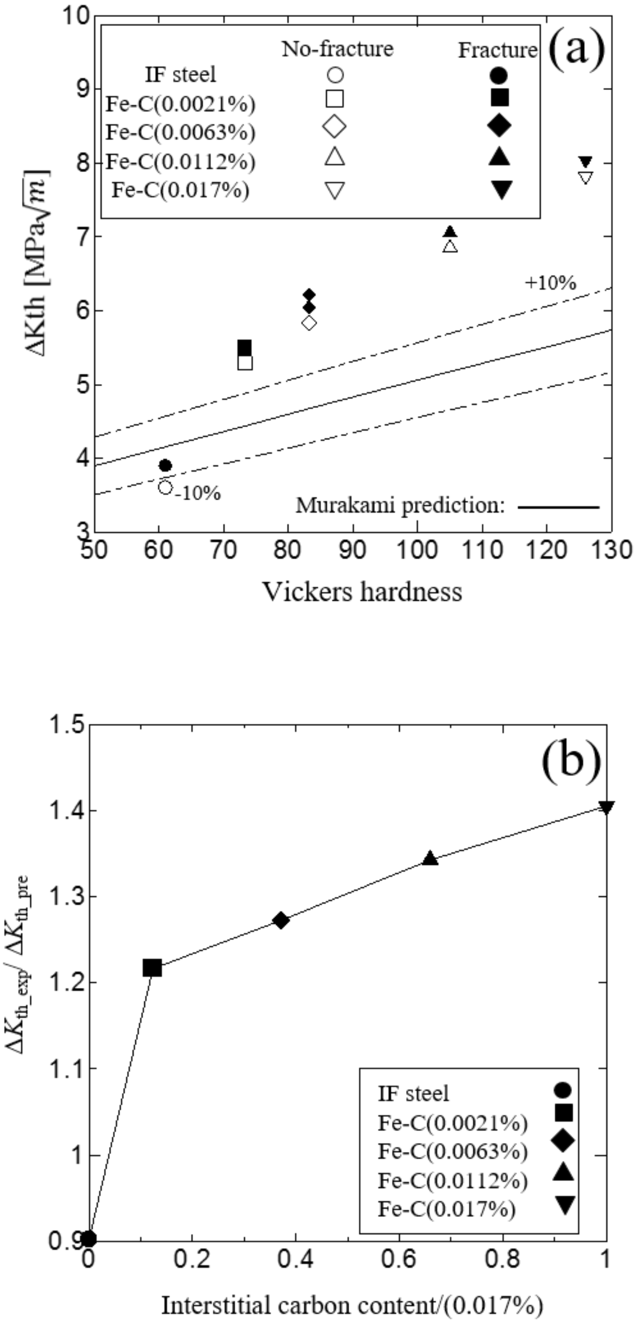

Fig. 4.1 The fatigue experimental data for the five steels used in this study: (a) ΔK_{th} values and (b) normalized ΔK_{th} values (IF and Fe-0.017C data results from Chapter 3)

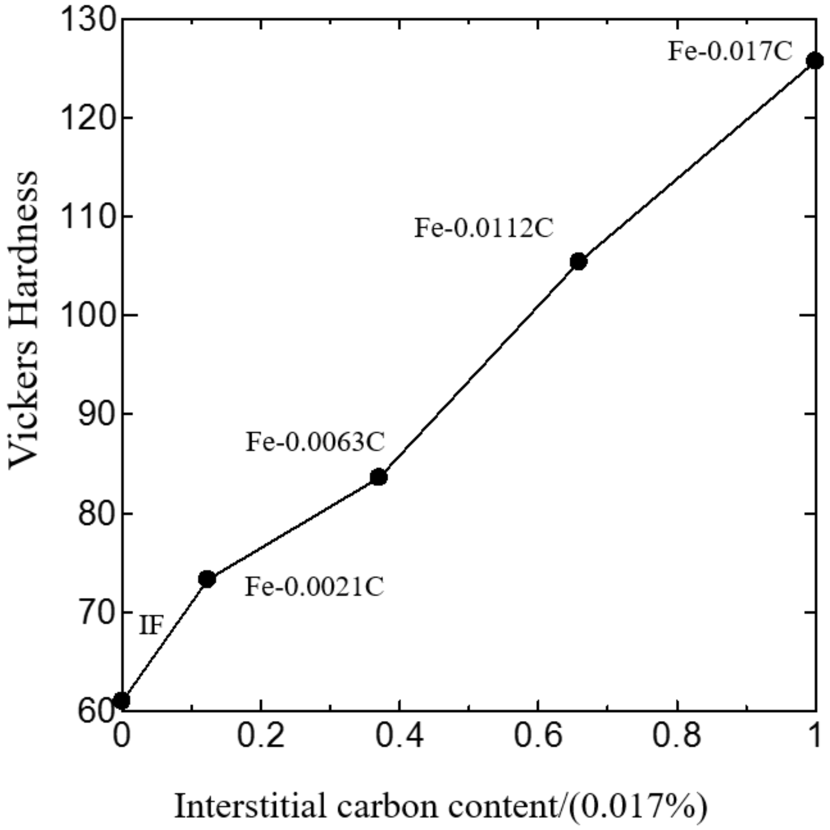

Fig. 4.2 The correlation between Vickers hardness and interstitial carbon content

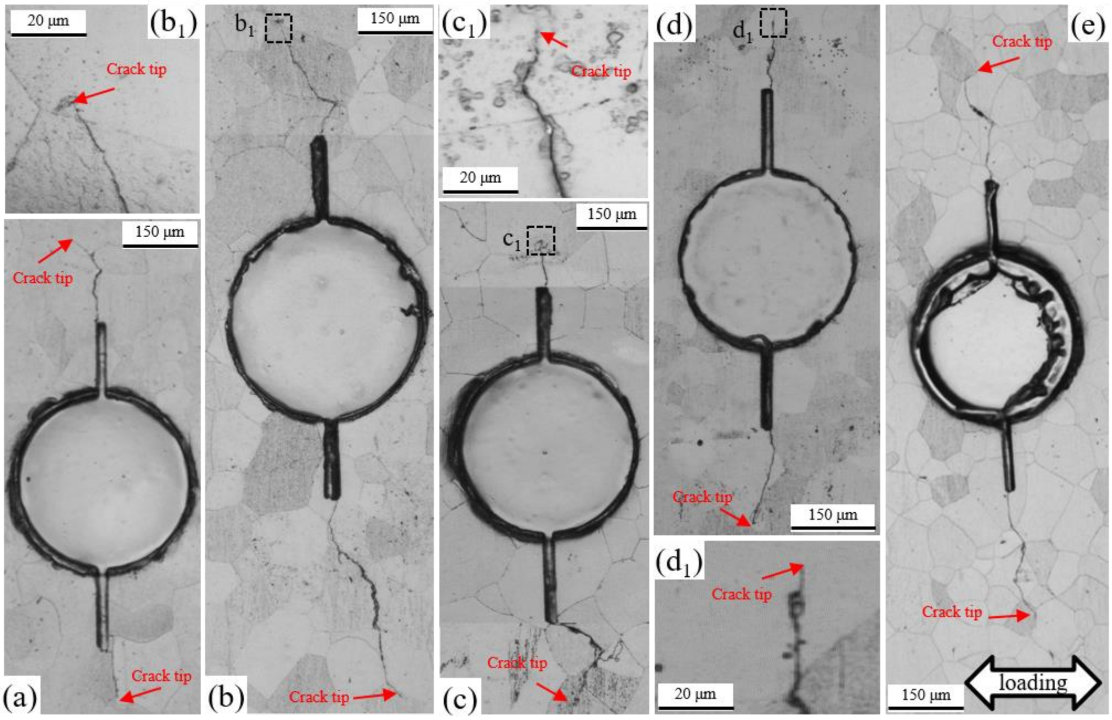

Fig. 4.3 Replica images of non-propagating specimens for the five steels used in the chapter: (a) IF steel (σ_a =87MPa); (b) Fe-0.0021C (σ_a =125MPa); (c) Fe-0.0063C (σ_a =138MPa); (d) Fe-0.0112C (σ_a =162MPa); and (e) Fe-0.017C (σ_a =185MPa) (IF and Fe-0.017C data results from Chapter 3)

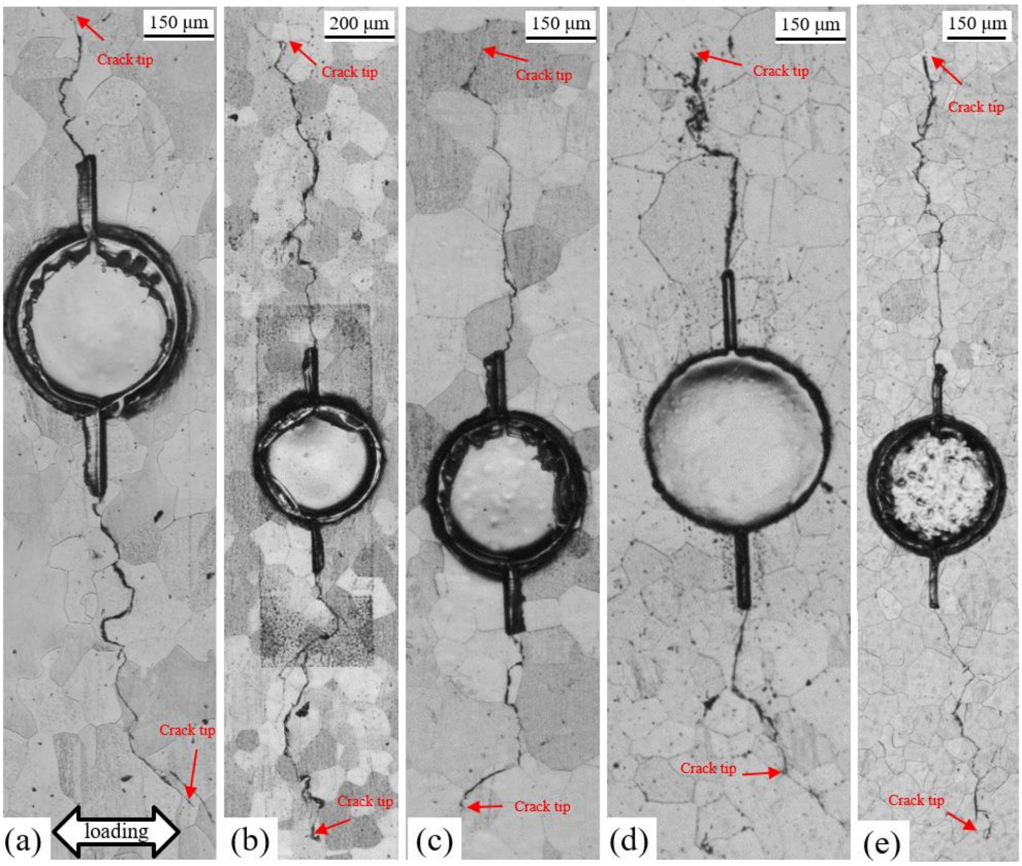

Fig. 4.4 Replica image of fracture specimens for the five steels used in this chapter: (a) IF steel (σ_a =90MPa N_f=1.1×10^6); (b) Fe-0.0021C (σ_a =130MPa N_f=1.1×10^6); (c) Fe-0.0063C (σ_a =143MPa N_f=4.2×10^6); (d) Fe-0.0112C(σ_a=167MPa N_f=3.2×10^6); and (e) Fe-0.017C (σ_a=190MPa N_f=1.8×10^6) (IF and Fe-0.017C data results from Chapter 3)

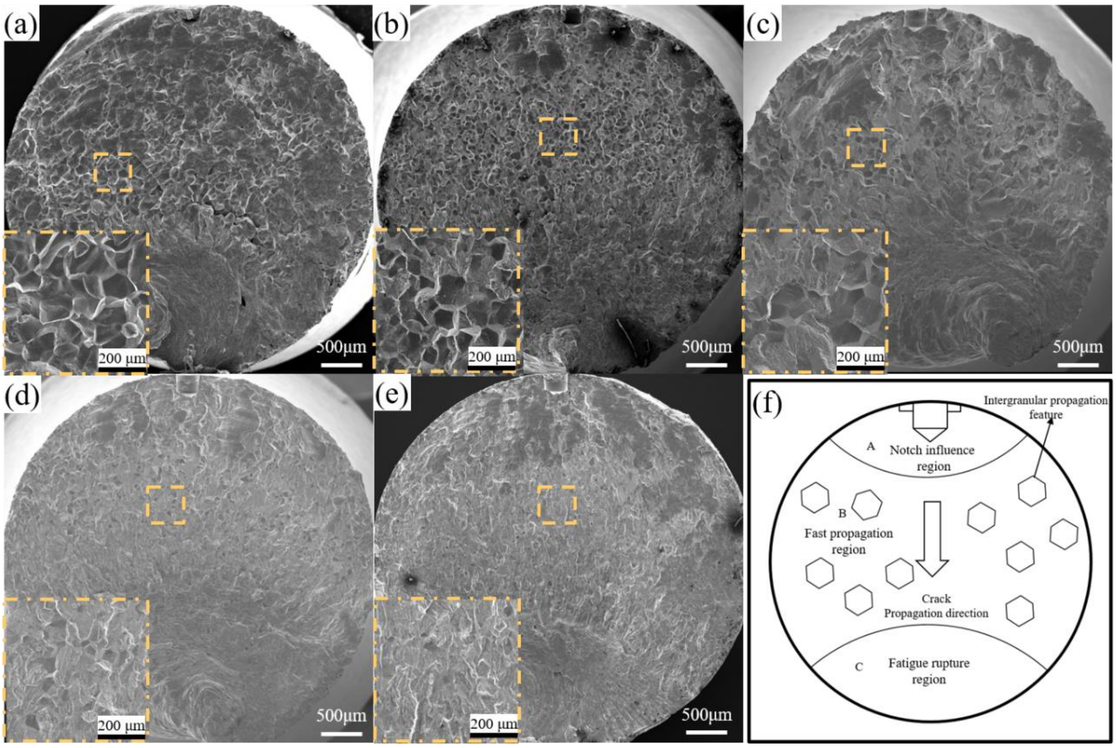

Fig. 4.5 SEM images of the fracture surface for the five steels used in this chapter and its schematic illustration of the fracture surface features: (a) IF steel (σ_a =90MPa N_f=1.1×10^6); (b) Fe-0.0021C (σ_a =130MPa N_f=1.1×10^6); (c) Fe-0.0063C (σ_a =143MPa N_f=4.2×10^6); (d) Fe-0.0112C(σ_a =167MPa N_f=3.2×10^6); (e) Fe-0.017C (σ_a =190MPa N_f=1.8×10^6); and (f) the schematic of the fracture surface features (IF and Fe-0.017C data results from Chapter 3)

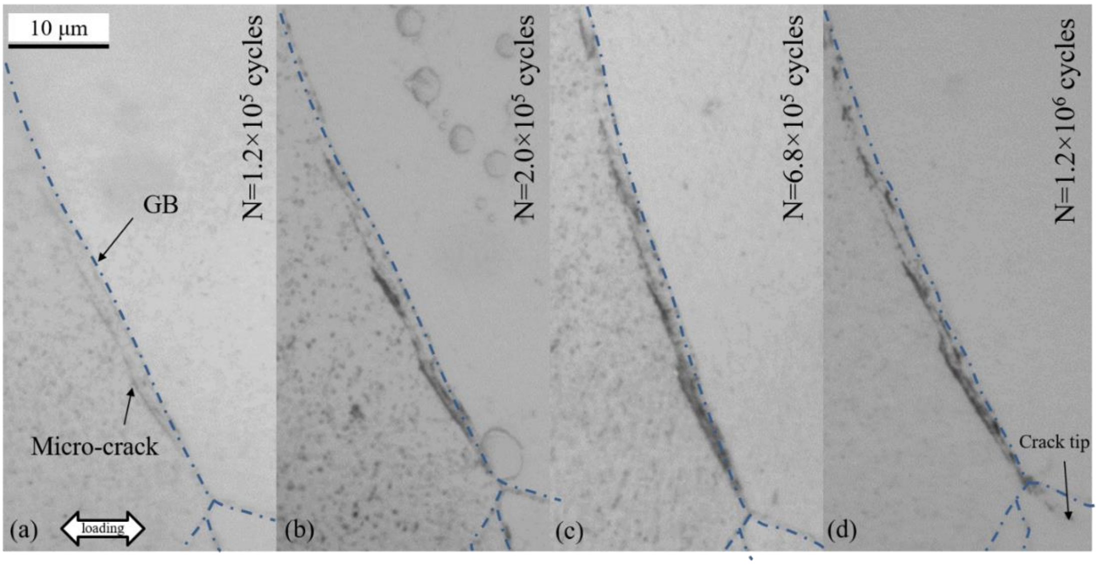

Fig. 4.6 Intergranular crack initiation mechanism of Fe-0.017C specimen with a FIB notch at 210MPa, presented in our previous work [1]: (a) N=1.2×10^5 cycles; (b) N=2.0×10^5 cycles; (c) N=6.8×10^5 cycles; and (d) N=1.2×10^6 cycles

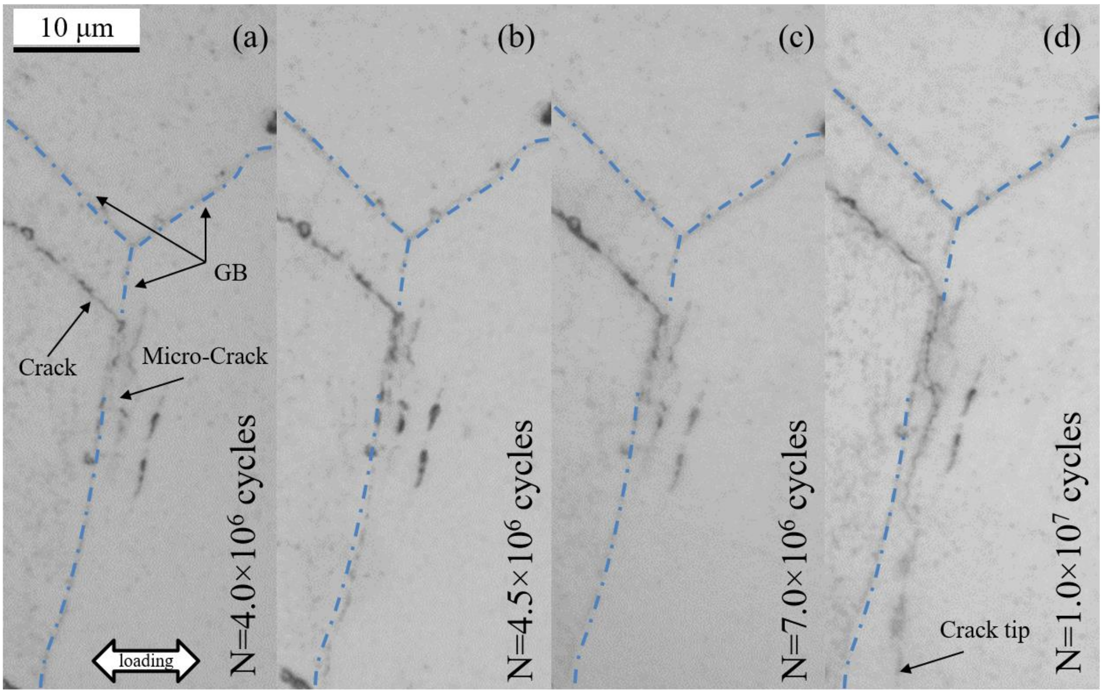

Fig. 4.7 Crack propagation mechanism through GBs of Fe-0.017C (σ_a =185MPa) for the specimens with non-propagating cracks shown in Fig. 4.3e: (a) N=4.0×10^6 cycles; (b) N=4.5×10^6 cycles; (c) N=7.0×10^6 cycles; and (d) N=1.0×10^7 cycles

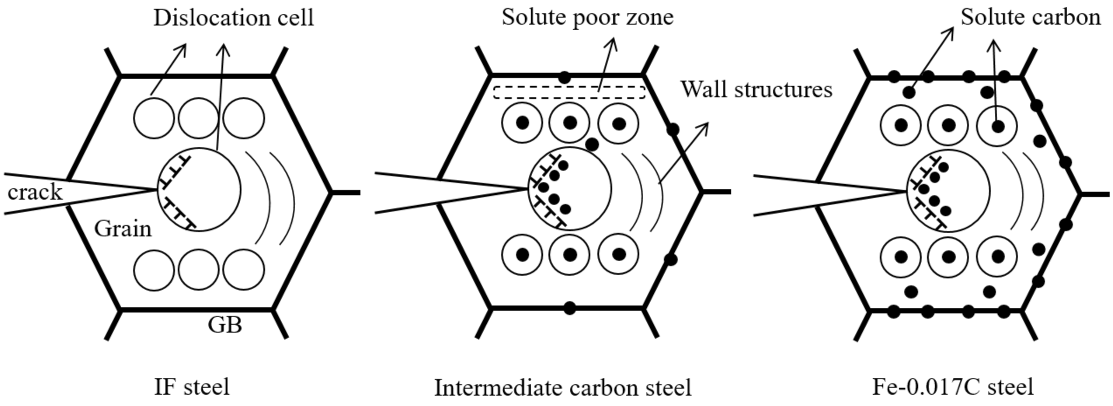

Fig. 4.8 Schematic of the solute content effect differences between the five steels used in this chapter

Table 4.1. Predicted and experimental mechanical properties of the five steels used in this chapter (IF and Fe-0.017C data results from Chapter 3)

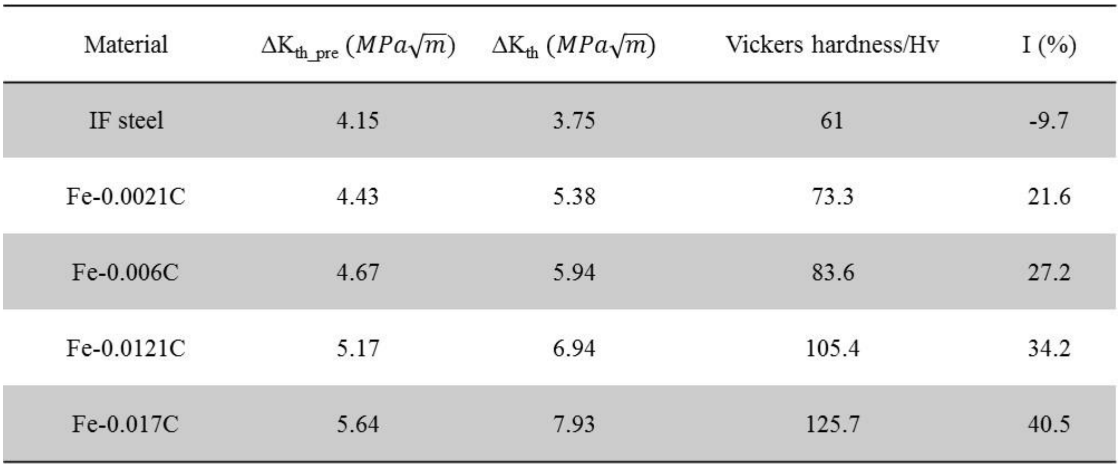

Material	ΔK_{th_pre} $(MPa\sqrt{m})$	ΔK_{th} $(MPa\sqrt{m})$	Vickers hardness/Hv	I (%)
IF steel	4.15	3.75	61	-9.7
Fe-0.0021C	4.43	5.38	73.3	21.6
Fe-0.006C	4.67	5.94	83.6	27.2
Fe-0.0121C	5.17	6.94	105.4	34.2
Fe-0.017C	5.64	7.93	125.7	40.5

CHAPTER 5. The analysis of transgranular fatigue crack resistance for Fe-0.017C containing supersaturated solute atom at different testing temperatures

5.1 Introduction

Clearly, the fatigue experiments in Chapter 3 and Chapter 4 are all conducted at room temperature. Nevertheless, temperature is one of another important factor to control the DSA hardening due to changing the solute diffusivity. When the working temperature is relatively high, the DSA hardening can be enhanced and the corresponding DSA temperature interval is called as the DSA regime [1-4]. Additionally, the fatigue test of Fe-0.017C does reveal remarkable transgranular fatigue crack resistance even at room temperature due to DSA hardening resulting from largest interstitial carbon content. Therefore, it is expected to further increase ΔK_{th} of Fe-0.017C at elevated temperature based on above analysis and the corresponding tests at different testing temperatures are carried out in this chapter.

5.2 Tension and fatigue experimental procedure

In this Chapter, two materials same as Chapter 3 are employed. The normal tension tests with strain rate 10^{-3} s^{-1} for IF and Fe-0.017C at temperatures varying from 293 *K* to 523 *K* are conducted. The geometry of tension test is illustrated in Fig. 2.3. Subsequently, the fatigue tests for two materials at two high temperatures 333 K and 433 K are carried out by using one tension-compression fatigue machine accompanying a high temperature chamber with a stress ratio of -1 and frequency of 35 Hz. The fatigue specimen shape at high temperatures is described in Fig. 5.1 and the micro-notch geometry and size are same as that at room temperature. Lastly, the extra tension tests for Fe-0.017C after aging treatment under different heating temperatures and testing temperatures are performed.

5.3 Experimental results and discussion

5.3.1 The temperature dependence of two steels in stress-strain curve

The stress-strain curves (S-S curve) for IF steel under 293 K, 333 K and 433 K are summarized in Fig. 5.2a, while the S-S curve for Fe-0.017C steels at temperatures changing from 293 K to 523 K are described in Fig. 5.2b. In the case of IF steel, the induced stress at same plastic strain reduces with the increase of working temperature as the dislocation motion is controlled by the thermal activation process. Specifically, thermal vibrations of the crystal atoms may assist the dislocation to overcome the obstacle during movement by using lower external force [5]. By contrary, higher flow stress do reveal in Fe-0.017C steel with almost 0.017% interstitial carbon content at higher temperatures varying from 333 K to 523 K under same plastic strain.

Furthermore, the serrations, one of the most important manifestations for DSA phenomenon, can also be found in Fe-0.017C steel and its elongation gradually decreases with the growth of working temperature. Additionally, the 0.2% proof stress and ultimate strength for both materials are revealed in Fig. 5.3. Obviously, not only the 0.2% proof stress but also ultimate strength of IF steel reduces with temperature increasing, while both properties of Fe-0.017C reveals positive temperature sensitivity. The opposite tendency of ultimate strength in Fe-0.017 is clearly attributed to DSA hardening and the relative temperature interval from 333 K to 523 K can be regarded as the DSA regime. Therefore, it can verify that DSA occurs at least in Fe-0.017C at high temperatures and IF does not have any DSA effect.

5.3.2 Fatigue performance of both steels at different testing temperatures

In fatigue test, only two working high temperatures, 333 K and 433 K, are selected and the corresponding fatigue results are used to compare with that at room temperature 293 K. The fatigue experimental data of both steels are summarized in Fig. 5.4 in detail. In terms of the S-N curves in IF steel in Fig. 5.4a, the knee point is always located at 10^7 cycles under all working temperatures, whereas the knee point of Fe-0.017C steel gradually transfers from the 10^6 to 10^7 cycles when the working temperature grows, which is one of characteristics for DSA hardening disappearance. As shown in Fig. 4b, the $\triangle K_{th}$ values of Fe-0.017C steel and IF steel at 293 K are 7.93 MPa$\sqrt{m}$ and 3.75 MPa$\sqrt{m}$, respectively resulting from Chapter 3 [6]. At 333 K temperature, the $\triangle K_{th}$ of Fe-0.017C steel is around 7.71 MPa$\sqrt{m}$ which is slightly smaller than that at 293 K, while significant reduction of $\triangle K_{th}$ manifests in IF steel close to 2.83 MPa$\sqrt{m}$. As the working temperature is increased to 433 K, both fatigue performance of two steels reveal remarkable decrease. In order to compare the fatigue strength between these two materials at elevated temperature, the ratio of $\triangle K_{th}$ value to that obtained at room temperature $\triangle K_{th\_RT}$ is used. It can be seen obviously from Fig. 5.4c that the fatigue strength of Fe-0.017C steel is always much larger than that of IF steel at both high temperatures.

The replica images of specimens with non-propagating crack at three temperatures for both steels are shown in Fig. 5.5. Clearly, all the fatigue cracks initiate from the FIB notch tip due to the stress concentration and then propagate as transgranular propagation behaviour for both IF and Fe-0.017C steel. After passing through one or more GBs, almost all fatigue crack finally stop in the grain interior rather than on the GBs. Namely, once the solute atoms exist in the grain interior, it is expected that the DSA mechanism can harden the material strength of plastic zone in the front of the crack tip.

5.3.3 Mechanical properties of Fe-0.017C after aging treatment

It is believed that supersaturated carbon in Fe-0.017C will gradually form carbon cluster or carbide such as cementite at elevated temperature. As described in Fig. 5.3b, the 0.2% proof stress of Fe-0.017C at 433 K is larger than that at 293 K (RT) presumably due to the carbon segregation to GBs or formation of fine carbide. Meanwhile, as the fatigue frequency is 35Hz, it will cost more than 3 days for non-propagating cracked specimen. Therefore, it is necessary to investigate the mechanical properties of Fe-0.017C steel in a period of 3 days at high temperatures. Another group of tension test at RT for Fe-0.017C steel with different heating time at 433 K is revealed in Fig. 5.6. Evidently, the 0.2% proof stress firstly increases from heating time 0 h to 2 h and then decreases with growth of heating time. By contrary, in terms of ultimate strength, there is no maximum in a period of 3 days. After heating specimen for more than 24 h, the material strength is significantly weaker than that without any heat treatment. In addition, tension tests at high temperatures were also conducted for Fe-0.017C steels after corresponding heat treatment. As can be seen from Fig. 5.7a clearly, although the tensile strength at 333 K with extra heat treatment is always lower than that without treatment, the yield strength is improved to some extent. In the case of working temperature at 433 K in Fig. 5.7b, however, both yield strength and ultimate strength become much weaker after relative aging treatment. Remarkably, serrations do disappear in the stress-strain curve both at 333 K and 433 K for specimen with extra treatment compared with those without treatment.

5.3.4 The analysis for temperature dependence of $\triangle K_{\mathrm{th}}$

Firstly, as mentioned above in section 5.3.3, it is obviously found that the precipitation in Fe-0.017C steel experiences the transition process from underaged to overaged state. More specifically, with the increase of temperature, the number of precipitates progressively grows as shown in Figs. 5.8(a-c). It can be seen from Fig. 5.8 that precipitate almost cannot be observed at RT both for fractured and non-fractured specimens, whereas a large amount of precipitates manifest in the specimen surfaces at high temperatures, especially for specimens at 433 K as described in Fig. 5.8c and Fig. 5.8f. Moreover, with the growth of aging time, the size of precipitate increases with a general loss in the strength of coherent strain after peak aging and the steel becomes softened to well below its maximum strength, such as the 0.2% proof stress in Fig. 5.6b [7]. Obviously, there is no maximum in ultimate strength with rise of aging time described in Fig. 5.6b probably due to gradual disappearance of DSA effect. Namely, there exists the competition among three kinds of hardening mechanism during fatigue test: solid solution hardening, DSA hardening and precipitation hardening. As the working time rises at elevated temperature, the former two kinds of hardening progressively weaken and the latter one is firstly enhanced and finally become impaired.

The Vickers hardness values measured for the specimens with non-propagating crack after fatigue test at three temperatures are summarized in Fig. 5.9. In the light of IF steel, there is no change for hardness after fatigue test, while the hardness of Fe-0.017C steel is risen after testing at 333 K and reduced at 433 K which exhibits the process from underaged hardening to overaged hardening. Apart from the measurement of mechanical properties, another direct evidence, as illustrated in Fig. 5.10 and Fig. 5.11, can be used to describe the softness of material properties in front of the fatigue crack tip. To be exact, the fracture surface can be divided into three parts as shown in Fig. 5.10a and Fig. 5.11a. The notch influence region around the micro-notch is regarded as Part I, Part II corresponds to fast propagation region which is not affected by initial notch geometry, and Part III is the final fracture region. Four observation areas (A-D) in Part II are selected to compare the fracture morphologies at three temperatures with each other. In terms of IF steel, due to lack of carbon segregation to GB at RT, intergranular cracking occurs predominantly as revealed in Fig. 5.10b. Except for that at RT, striation can always be observed easily at four areas under 333 K and 433 K. In comparison, similar fracture features are found in Fe-0.017C steel at 433K. For the case of 333 K, most fracture morphologies at area A and B close to Part I is shown as Fig. 5.11c rather than striation morphologies in Fig. 5.11f. In fact, it is believed that striation usually prefers to manifest in soft material, such as aluminium and magnesium, as large plastic deformation can be formed during fatigue propagation [8]. According to the tension tests in Fig. 5.2a, IF steel, whose strength is similar to normal aluminium alloy [8], is sufficiently soft to form visible striation. Therefore, it is reasonable to deduce that the material strength of Fe-0.017C steel at 433 K is weakened. Compared with Fe-0.017C steel at 433 K in Fig. 5.11f, the striation of Fe-0.017C at 333 K in area A, as shown in Fig. 5.11c, may be removed due to friction between two crack surfaces with low crack growth rate and become invisible. In a word, the material properties, i.e. yield strength, of Fe-0.017C in front of the crack tip at 433 K is impaired. It is reported that the yield strain in front of the crack tip is a crucial parameter to control the effect of plasticity-induced crack closure (PICC) for small crack and higher yield strain can result in higher ΔK_{th} value [9]. Similar conclusion can be made according to the Murakami equation in Eq. (3.2) where the larger Vickers hardness the stronger fatigue performance. That is to say, the contribution of PICC to ΔK_{th} for IF steel reduces significantly from RT to 433 K, while that for Fe-0.017C steel changes slight from RT to 333 K and also decrease prominently from 333 K to 433 K, which is consistent with its temperature dependence of ΔK_{th} in Fig. 5.4.

Besides the striation observation, another characteristic in fracture surface of Fe-

0.017C can be observed under high temperature, especially at low stress level as shown in Fig. 5.12. The corresponding fracture images in Fig. 5.12 are indicated by arrows in Fig. 5.4a. At a low stress level and a temperature of 333 K or 433 K, microstructure features resembling those observed in stage I crack propagation can be detected, particularly at the higher temperature of 433 K. In comparison, these features were only barely observed at a higher stress level in the same observation area, with isolated stage I-like features visible in Fig 5.12d. On the contrary, these features were also barely detected in our previous research, conducted at room temperature [10]. The stage I-like features could be caused by the shearable nature of the precipitates at a low ΔK range [11]. As the working temperature for the fatigue test was not as high as much enough, the cementite precipitate size was fine and therefore shearable. Furthermore, only a single slip system can be activated at a low stress level. Therefore, the corresponding appearance of stage I-like features close to the initial notch often occurs at elevated temperatures and low stress levels, as shown in Fig 5.12. These features cannot be detected in regions located far from the notch position under any temperature or stress level.

Based on these kinds of characteristic in fracture surface in Fe-0.017C and change of fatigue crack propagation behavior of IF steel from intergranluar to transgranular behavior with temperature growth, it is interesting to further investigate the fracture morphologies near the micro-notch for both materials. Consequently, the three-dimensional fracture morphologies of two materials at three temperatures are built in Fig. 5.13. Specifically, the asperity in Fe-0.017C steel at RT is much less than that of

IF due to intergranular cracking in IF steel. However, with the growth of working temperature, the crack propagation path of Fe-0.017C becomes much more tortuous than that under RT as a result of formation of finely shearable cementite. In comparison, with the transformation of crack propagation behaviour of IF steel, the asperity of fracture surfaces progressively become small. Accordingly, the roughness-induced crack closure (RICC) increasingly plays an important role in ΔK_{th} value, especially at 333 K and 433 K for Fe-0.017C steel.

In summary, there always exists large difference between Fe-0.017C with 0.017% solute carbon and IF steel without any solute carbon in terms of ΔK_{th} at three temperatures due to different controlling factors. Solid solution hardening and DSA hardening, resulting in PICC contribution to ΔK_{th}, is the crucial factor at RT, while three kinds of hardening mechanisms including under-aged precipitation hardening play a key role in ΔK_{th} at 333 K. Comparatively, the extent of asperity of fracture surface, leading RICC contribution to ΔK_{th}, and over-aged precipitation hardening result in stronger fatigue strength of Fe-0.017C steel than IF steel at 433 K. Nevertheless, the DSA capacity in Fe-0.017C steel is exhausted as a result of solute carbon segregation and a large amount of fine cementites.

5.4 Section conclusion

The temperature dependence of tension properties for Fe-0.017C and IF steels were examined by using three temperatures and the threshold stress intensity factors ranges of a small crack under three temperatures were also determined by using tension-tension fatigue machine with a high temperature chamber. Furthermore, the mechanical properties of Fe-0.017C steel in a period of 3 days at high temperatures were investigated as well. The following conclusion can be made:

1. The DSA phenomenon can be observed at elevated temperature in stress-strain curve for Fe-0.017C, while IF steel does not have.
2. The under-aged hardening for Fe-0.017C steel occurs at 333 K, whereas the over-aged hardening reveals at 433 K;
3. The ΔK_{th} of IF steel reduces significantly from RT to 433 K, whilst that for Fe-0.017C steel changes slight from RT to 333 K and also decrease prominently from 333 K to 433 K
4. The large difference of ΔK_{th} between two materials at three temperatures is as a result of different controlling factors: solid-solution hardening and DSA hardening at RT; weakened solid-solution hardening, DSA hardening and under-aged precipitation hardening at 333K; the roughness of fracture surface and over-aged hardening at 433 K.
5. Due to a large amount of fine cementite precipitation during fatigue test at high temperature, the DSA capacity in Fe-0.017C steel disappears due to exhaustion of large amount of interstitial carbon, hence, the contribution of DSA hardening to PICC enhancement gradually disappears and the corresponding fatigue performance, i.e. ΔK_{th} for micro-notch, declines sharply.

5.5 Reference

[1] C. Cui, Y. Gu, Y. Yuan, H. Harada, Dynamic strain aging in a new Ni–Co base superalloy, Scripta Materialia, 64 (2011) 502-505.
[2] M. Srinivas, G. Malakondaiah, K.L. Murty, P.R. Rao, Fracture toughness in the dynamic strain ageing regime, Scripta metallurgica et materialia, 25 (1991) 2585-2588.
[3] V. Srinivasan, M. Valsan, R. Sandhya, K.B.S. Rao, S. Mannan, D. Sastry, High temperature time-dependent low cycle fatigue behaviour of a type 316L (N) stainless steel, International Journal of Fatigue, 21 (1999) 11-21.
[4] S. Zhu, J. Nie, Serrated flow and tensile properties of a Mg–Y–Nd alloy, Scripta Materialia, 50 (2004) 51-55.
[5] D. Hull, D.J. Bacon, Introduction to dislocations, Butterworth-Heinemann, 2001.
[6] B. Li, M. Koyama, E. Sakurada, N. Yoshimura, K. Ushioda, H. Noguchi, Underlying interstitial carbon concentration dependence of transgranular fatigue crack resistance in Fe-C ferritic steels: The kinetic effect viewpoint, International Journal of Fatigue, 98 (2017) 101-110.
[7] R. Abbaschian, R.E. Reed-Hill, Physical metallurgy principles, Cengage Learning, 2008.
[8] S. Suresh, Fatigue of materials, Cambridge university press, 1998.
[9] N. Fukumura, T. Suzuki, S. Hamada, K. Tsuzaki, H. Noguchi, Mechanical examination of crack length dependency and material dependency on threshold stress intensity factor range with Dugdale model, Engineering Fracture Mechanics, 135 (2015) 168-186.
[10] B. Li, M. Koyama, E. Sakurada, N. Yoshimura, K. Ushioda, H. Noguchi, Potential Resistance to Transgranular Fatigue Crack Growth of Fe-C alloy with a Supersaturated Carbon Clarified through FIB Micro-notching Technique, International Journal of Fatigue, (2016).
[11] J. Petit, C. Sarrazin-Baudoux, Some critical aspects of low rate fatigue crack propagation in metallic materials, International Journal of Fatigue, 32 (2010) 962-970.

5.6 Figures and tables

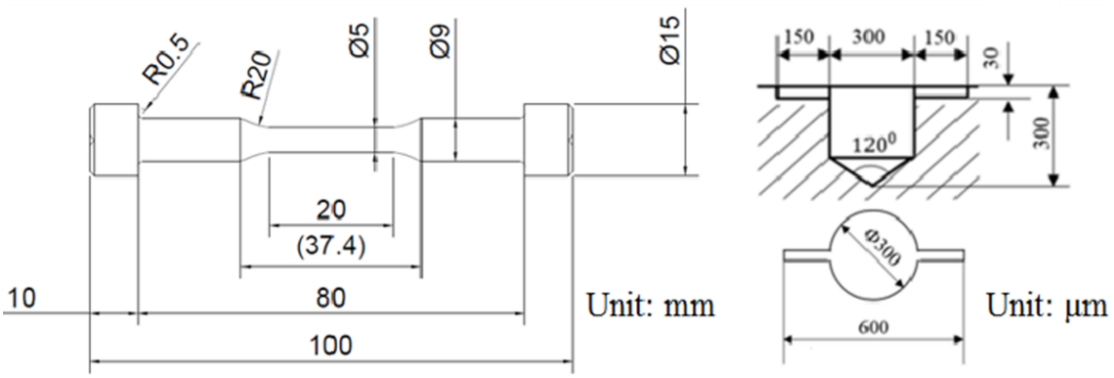

Fig. 5.1. The geometry of fatigue test specimen at high temperatures (notch shape and size are same as that at room temperature)

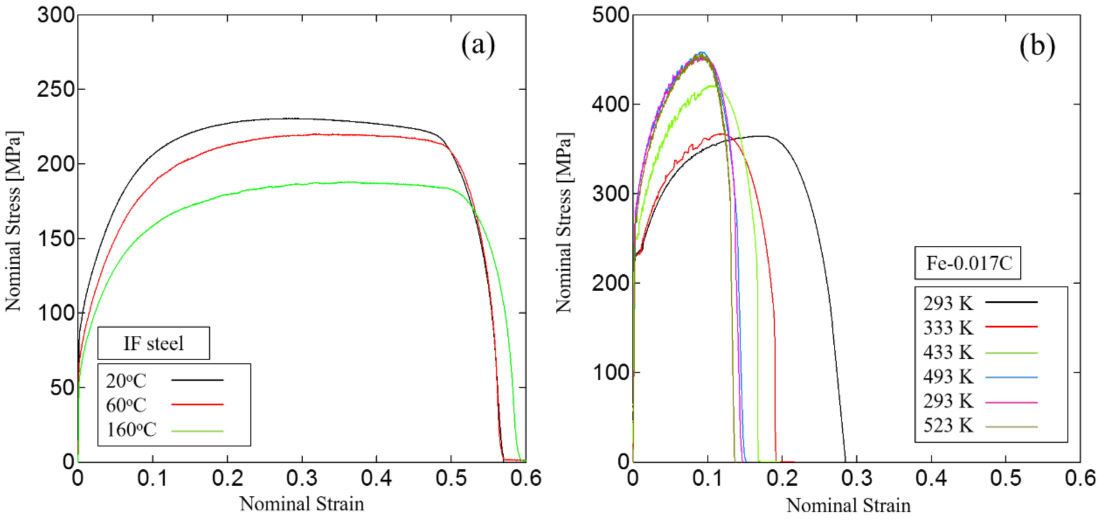

Fig. 5.2. The stress-strain curves for two materials at different testing temperatures with strain rate 10^{-3} s^{-1} (The results at room temperature results from Chapter 2)

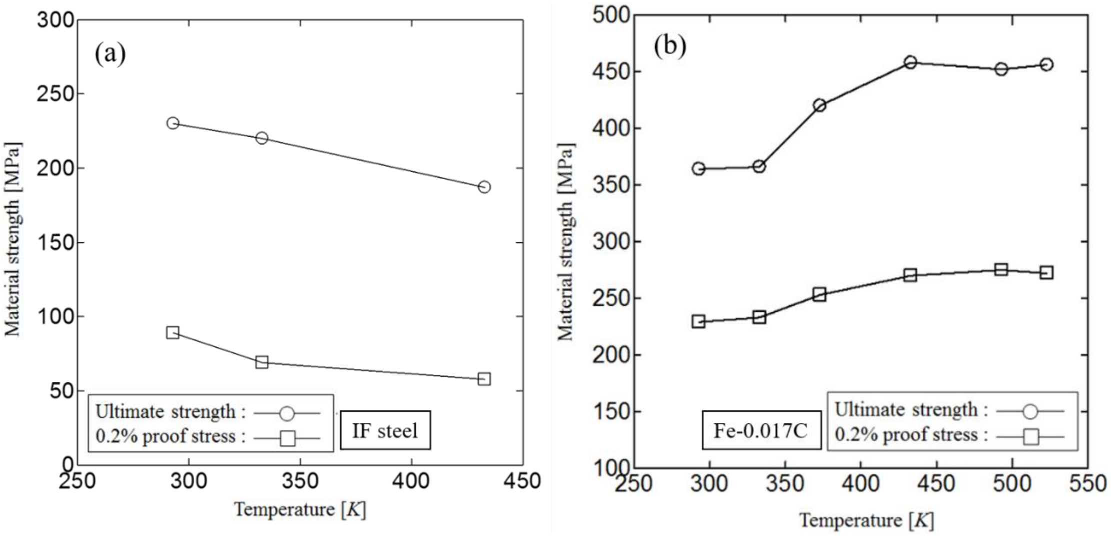

Fig. 5.3. The temperature dependence in tension test: (a) IF steel; (b) Fe-0.017C

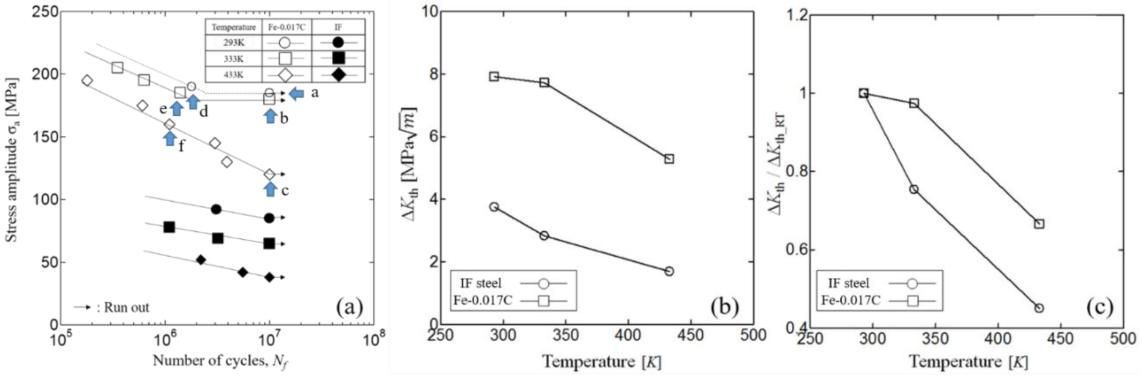

Fig. 5.4 The fatigue experimental data for these two materials used in this chapter: (a) S-N curves; (b) ΔK_{th} vs temperature; (c) Normalized ΔK_{th} vs temperature

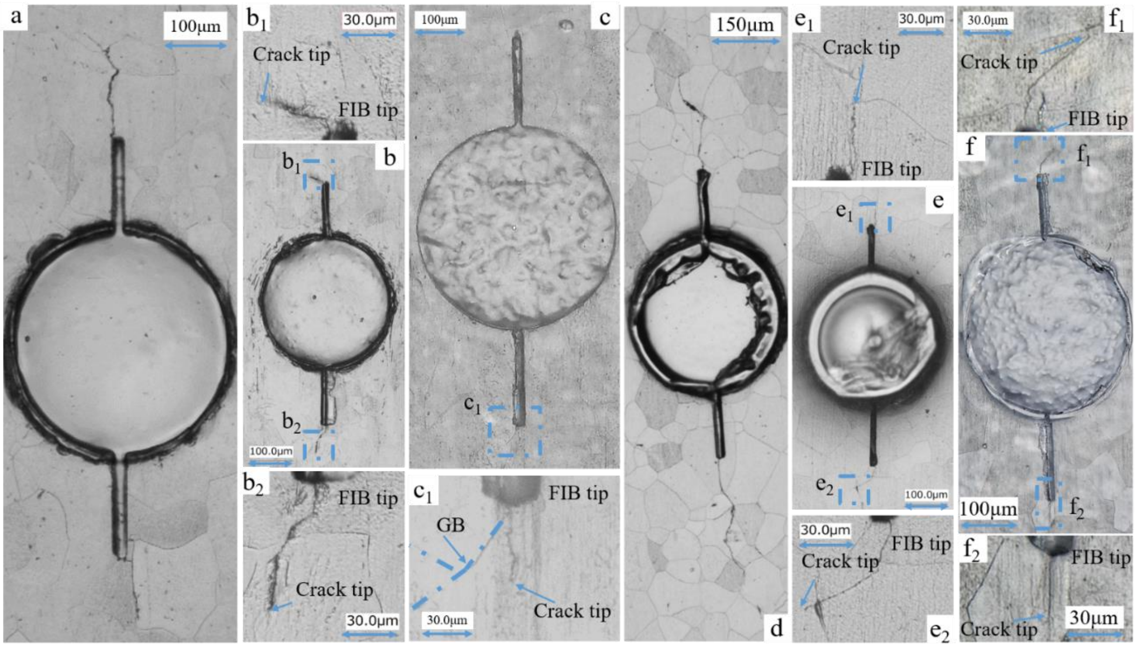

Fig. 5.5 Replica images of non-propagating specimens for two steels used in the study at different temperatures: (a) IF steel (T =293K); (b) IF steel (T =333K); (c) IF steel (T =433K); (d) Fe-0.017C (T =293K); (e) Fe-0.017C (T =333K); and (f) Fe-0.017C (T =433K); (The results at room temperature results from Chapter 3)

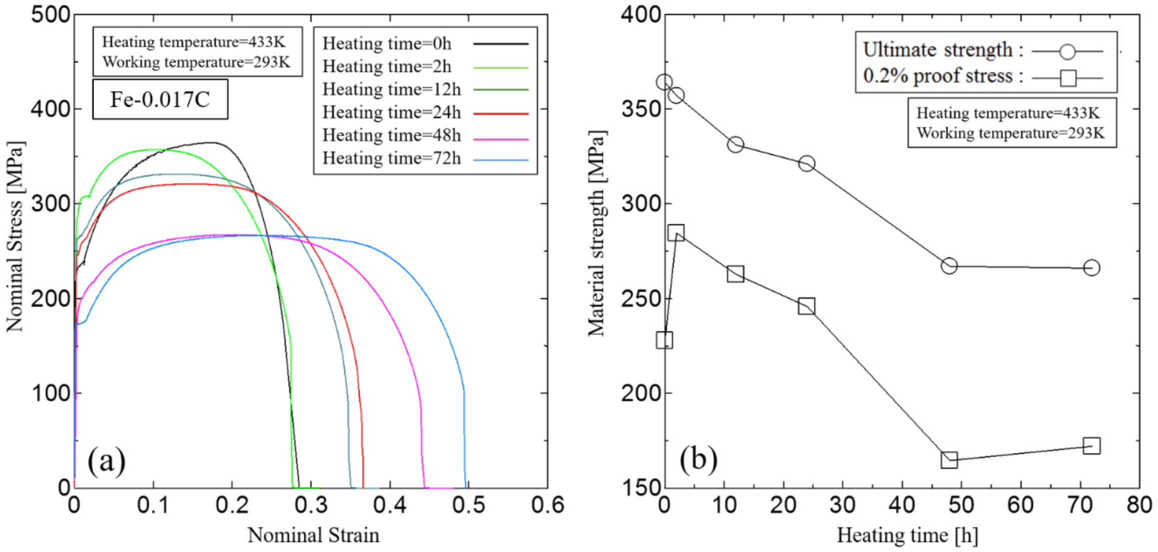

Fig. 5.6 The tension result with strain rate 10^{-3} s^{-1} in Fe-0.017C steel after corresponding heat treatment: (a) S-S curves at working temperature 293K with different heating time; (b) tension properties vs heating time

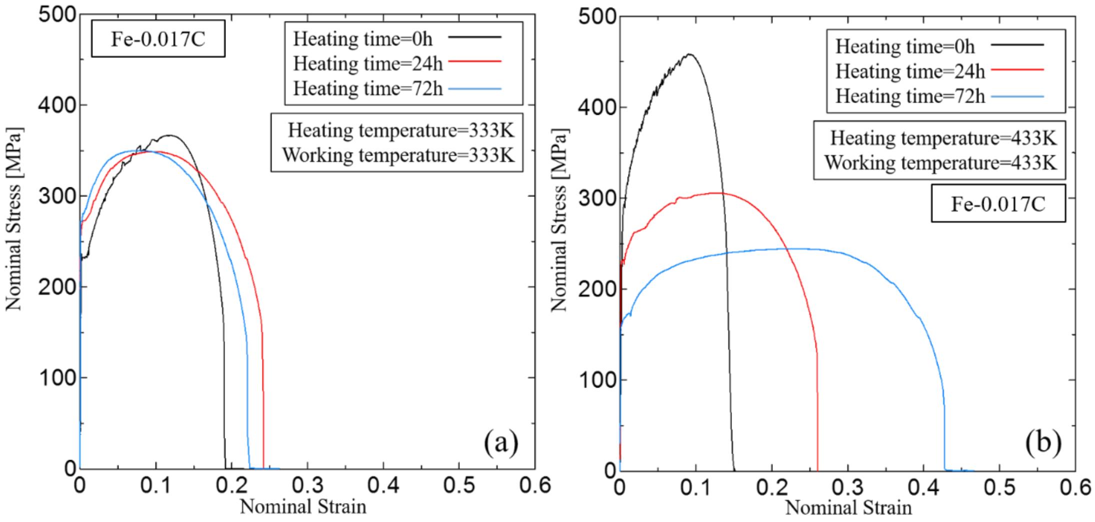

Fig. 5.7 The tension result with strain rate 10^{-3} s^{-1} in Fe-0.017C steel after corresponding heat treatment: (a) S-S curves at working temperature 333K; (b) S-S curves at working temperature 433K

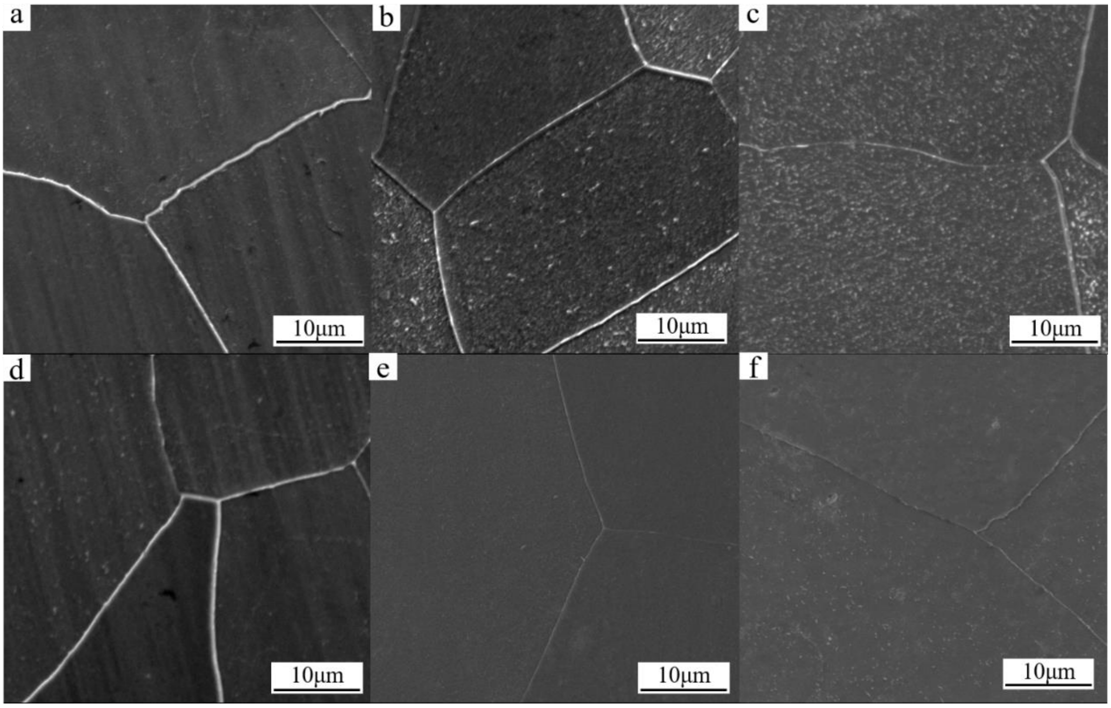

Fig. 5.8 The microstructures in Fe-0.017C steel after fatigue test in Fig. 5.4a: (a) specimen a; (b) specimen b; (c) specimen c; (d) specimen d; (e) specimen e; (f) specimen f;

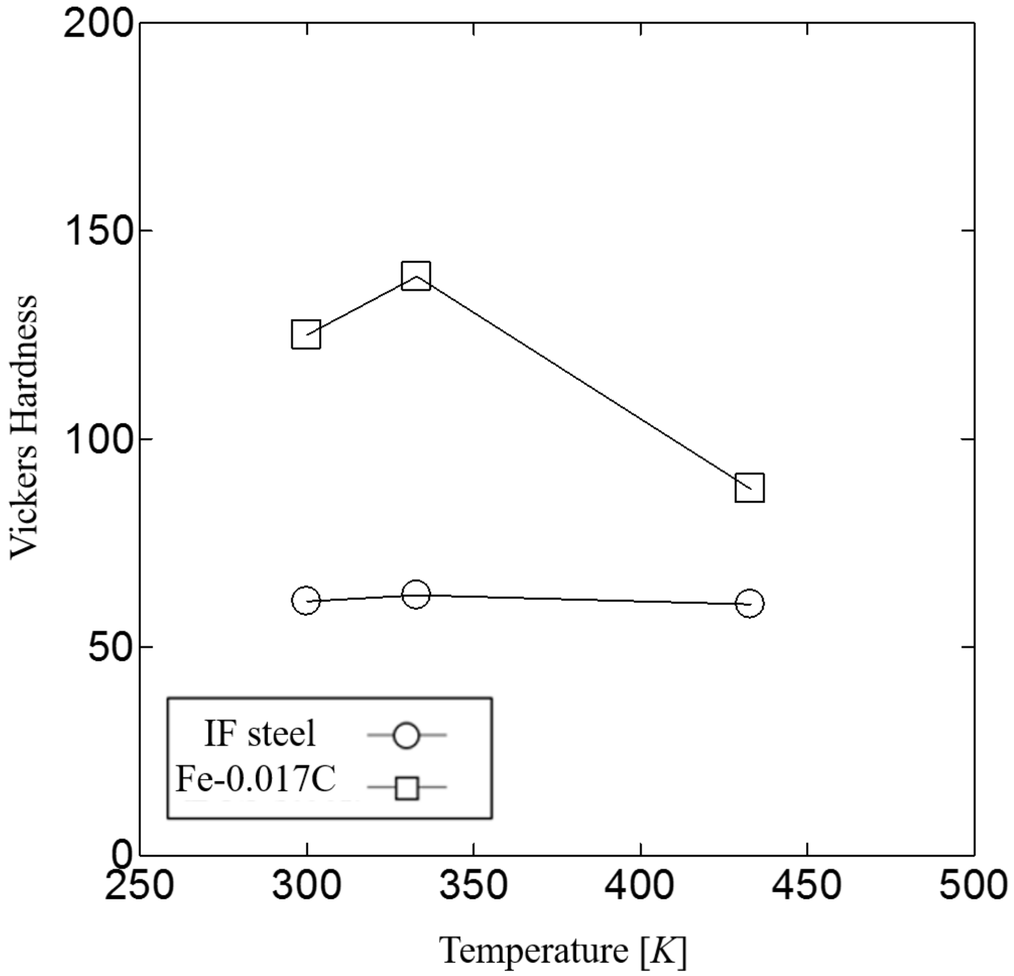

Fig. 5.9 The correlation between Vickers hardness of non-fractured specimen measured after test and working temperature.

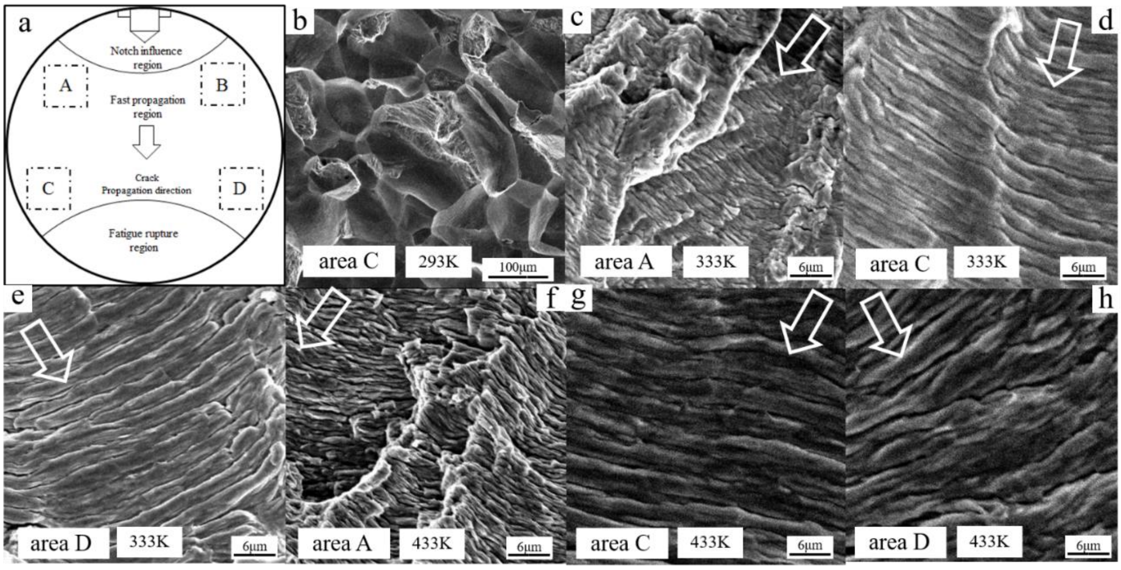

Fig. 5.10. SEM images of specimens for IF steel under different temperatures. (a) Schematic of fracture surface observation area. (b) Specimen tested at 293 K at area D (92MPa); (c) Specimen tested at 333 K at area A (69MPa); (d) Specimen tested at 333 K at area C (69MPa); (e) Specimen tested at 333 K at area D (69MPa); (f) Specimen tested at 433 K at area A (42MPa); (g) Specimen tested at 433 K at area C (42MPa); (h) Specimen tested at 433 K at area D (42MPa);

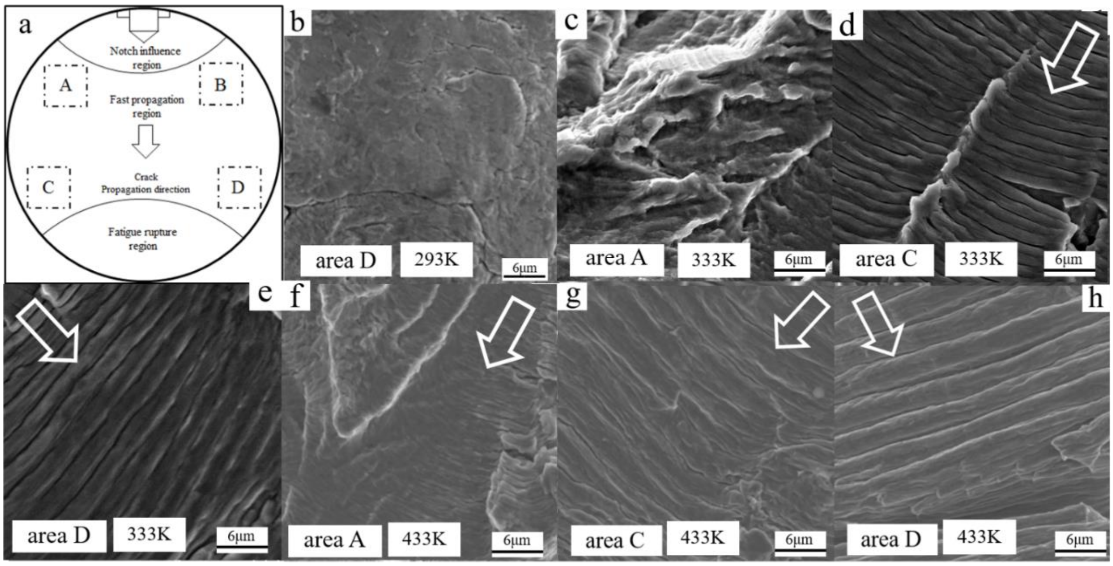

Fig. 5.11. SEM images of specimens for Fe-0.017C steel under different temperatures. (a) Schematic of fracture surface observation area. (b) Specimen tested at 293 K at area D (190MPa); (c) Specimen tested at 333 K at area A (185MPa); (d) Specimen tested at 333 K at area C (185MPa); (e) Specimen tested at 333 K at area D (185MPa); (f) Specimen tested at 433 K at area A (130MPa); (g) Specimen tested at 433 K at area C (130MPa); (h) Specimen tested at 433 K at area D (130MPa);

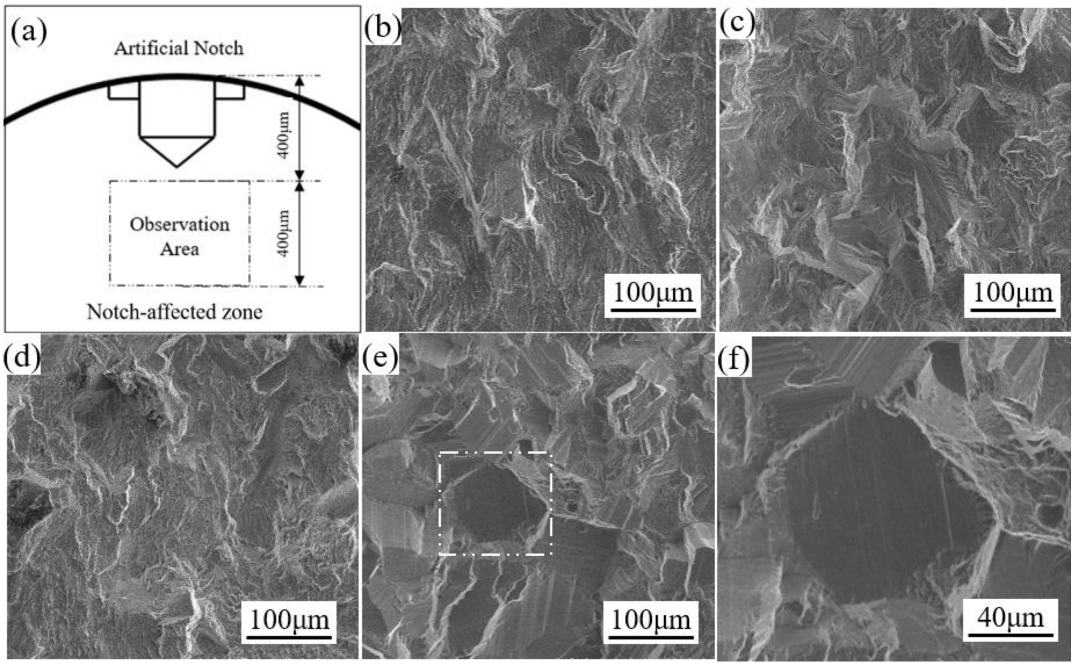

Fig. 5.12. Scanning electron microscopy (SEM) images of specimens under elevated temperatures. (a) Schematic of fracture surface observation area. (b) Specimen tested at a high stress level (205 MPa) at 333 K. (c) Specimen tested at a low stress level (185 MPa) at 333 K. (d) Specimen tested at a high stress level (195 MPa) at 433 K. (e) Specimen tested at a low stress level (145 MPa) at 433 K. (f) A magnified image of Fig 5.12e. Note that S-N curves for the specimens shown in images b–f are displayed in Fig 5.4a.

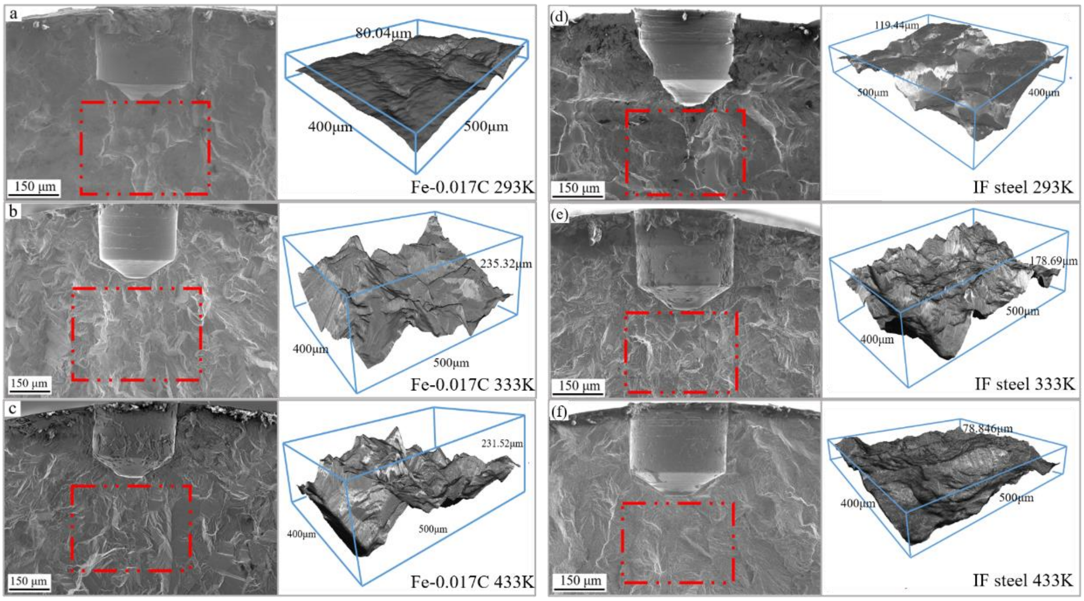

Fig. 5.13. The three-dimensional morphologies of two steels for fractured specimens near notch. (a) Fe-0.017C tested at 293 K (at 190MPa); (b) Fe-0.017C tested at 333 K (at 185MPa); (c) Fe-0.017C tested at 433 K (at 130MPa); (d) IF tested at 293 K (92MPa); (e) IF tested at 333 K (69MPa); (f) IF tested at 433 K (42MPa);

CHAPTER 6. General conclusion

In order to analyze the solute carbon concentration dependence of fatigue performance for ferritic steels, the relative tension and fatigue tests, both at room temperature and high temperature, were conducted and the corresponding threshold stress intensity factor ranges of ferritic steels with different solute carbon contents were examined. The detailed information and conclusion were shown as followed:

Initial investigations have been done for Fe-0.017C steel with almost 0.017% interstitial carbon content and IF steel without any solute carbon in comparison by using rotating bending fatigue machine at room temperature. Murakami equation to predict the threshold stress intensity factor ranges of two materials is used as the reference tool so that it could reflect the DSA effect in Fe-0.017C steel. Three micro-notches with different notch sizes, varying from 100 μm to 337 μm, are used for fatigue tests. However, in terms of notch sizes for Fe-0.017C steel, 100 μm and 227 μm, the specimens does not become fracture even though the stress amplitude is increased to 210MPa which was the fatigue limit of smooth specimen. Finally, the threshold stress intensity factor ranges of Fe-0.017C steel is determined by using the notch size 337 μm with the value of 7.93 MPa$\sqrt{m}$, which is around 40.5% higher than that of predicted result. By contrary, the stress intensity factor ranges of IF steel with three kinds of notch sizes can all be measured which were all close to the predicted value by Murakami equation. The large prediction error in Fe-0.017C is presumably attributed to improvement of PICC contribution originating from the DSA effect.

Subsequently, the fatigue test for another three ferritic steels, five steels in total, with different solute carbon contents are also carried out at room temperature by using same rotating bending fatigue machine. The stress intensity factor ranges of these five steels with notch size 337 μm increases, firstly steeply and then moderately, with the growth of solute carbon concentration. This phenomenon is probably due to that DSA only strongly hardened the material in grain interior in low solute carbon steel, such as Fe-0.0012C steel, while solute carbon gradually segregates to grain boundary and hardens the solute poor zone at the vicinity of grain boundary with the rise of solute carbon concentration so that the further improvement of stress intensity factor ranges can be acquired.

Lastly, the mixture influence of solute carbon concentration and temperature on fatigue performance of ferritic steels is investigated by using tension-compression fatigue machines with stress ratio -1 and frequency 35Hz. According to the tension test, serration obviously occurs at temperature 333 K and 433 K for Fe-0.017C steel rather than IF because of DSA influence. Nevertheless, the threshold stress intensity factor ranges of Fe-0.017C is not improved more or less at high temperature 433 K, oppositely, it reduces significantly compared with the results at room temperature which is attributed to the progressive disappearance of DSA effect. Furthermore, the mechanical properties of Fe-0.017C steel after aging treatment are also investigated which reflects the transition process from under-aged state to over-aged state during fatigue test. The fracture surfaces both for two steels under different temperature are observed and three-dimensional morphologies are built which reveals the different asperities of fracture surface near the micro-notch. Obviously, the material strength at high temperature of Fe-0.017C is weakened due to the gradual disappearance of DSA hardening and over-aging hardening, which results in the reduction in PICC influence. Additionally, the fatigue performance of Fe-0.017C is always much higher than that of IF steel at different temperatures because of different reasons: At room temperature, because of the solid solution hardening and DSA effect, leading to the PICC contribution, the transgranular fatigue crack resistance in Fe-0.017C is greater. Under 333 K, three kinds of hardening mechanisms including the under-aged hardening played critical role, while roughness induced crack closure and over-aged hardening are attributed at 433 K.

In conclusion, the higher solute carbon content in ferritic steel at room temperature has the larger transgranular fatigue crack resistance reveals. Despite weakened fatigue crack resistance is manifested at high temperature, it is expected to improve it by suppressing the precipitation to some extent and conserving the tortuous crack path behavior at high temperature.

Acknowledgement

This study was conducted in the Solid Mechanics Laboratory, Department of Mechanical Engineering, Kyushu University, Japan. Firstly, I am very grateful for my supervisor, Professor Hiroshi Noguchi. During my Phd period, he gave me many valuable suggestions and guidance for my study and much help for my life in Japan. I actually feel he is a very kind Professor although he sometimes do not know how to express himself in English and always does his research in office without any other entertainment. I also appreciate the valuable suggestion from Professor Kaneaki Tsuzaki and Professor Hiroyuki Toda for my Ph. D thesis. I also want to express my gratitude to Assistant Professor Motomichi Koyama for his deep discussion, valuable suggestions, pivotal modification for my paper and his joke and humor in our Phd life. Additionally, I want to extent my thanks to Associate Professor Shigeru Hamada for his help and instruction in my experiment and Mrs. Masako Kadota, secretary in our lab, for her care and help in my Japanese life.

In addition, I want to thanks Dr. Eisaku Sakurada and Mr. Nobuyuki Yoshimura from Nippon steel company for preparing perfect experimental materials. I would like to thanks my friends in Solid Mechanics Laboratory. Thanks for their guidance in experiment, deep discussion about research, happy moment in our party and wonderful communication about our cultures.

I really appreciate the financial support from China Scholarship Council (CSC) for my all living cost and tuition fee in Japan during Phd period. Finally, Special acknowledgement are made to my parents. Thanks to their encouragement, education and parenting for the past 28 years old, I can always live positively, healthy, happily and carefreely. Because of their suggestions and understanding in my life, I can always make a better and righter choice for my career. At the end of last year, my father experienced operation and chemotherapy. Fortunately, all the treatments were successfully. Now, I have already graduated and it is time for me to go back home and take good care of them. Everything will be alright! 頑張ります！

李 博川 LI BOCHUAN

Written in a Sunny day at Kyushu University, Fukuoka, Japan, May 2017